Measurement of Water Vapor Diffusion in Nanoscale Polymer Films by Frequency-Domain Probe Beam Deflection

Xu Xie,[1*] Jordan M. Dennison,[2] Jungwoo Shin,[1] Zhu Diao,[1] David G. Cahill[1*]

[1]*Department of Materials Science and Engineering, Frederick Seitz Materials Research Laboratory, University of Illinois at Urbana-Champaign, Urbana, Illinois 61801, USA.*

[2]*Department of Chemistry, University of Illinois at Urbana-Champaign, Urbana, Illinois 61801, USA.*

We developed an optical pump-probe technique, frequency-domain probe beam deflection (FD-PBD), to measure the diffusion of water vapor in nanoscale polymer films with microsecond temporal resolution and micrometer spatial resolution. We describe the quantitative model of beam deflection for multilayer structures, the experimental approach, and the application of FD-PBD to measure the diffusivity (D_m) of saturated water vapor in various glassy polymer films including polyimide (PI, D_m=7.0x10^{-13} m^2 s^{-1}), Poly(methyl methacrylate) (PMMA, D_m= 1.2x10^{-12} m^2 s^{-1}), poly-(vinylpyrrolidone) (PVP, D_m= 1.7 x10^{-12} m^2 s^{-1}) and cellulose acetate (CA, D_m=2.6 x10^{-11} m^2 s^{-1}), and the piperazine/ trimesoyl chloride (PIP/TMC, D_m=9x10^{-11} m^2 s^{-1}) nanofiltration membrane synthesized by interfacial polymerization. The uncertainty of the measurements is typically ≈ 8%.

I. INTRODUCTION

Understanding and controlling the diffusion of water vapor in polymer thin films is important for food packaging,[1] electronics encapsulation,[2] protective coatings,[3] fuel cells[4], and membrane dehumidification and gas separations.[5] For these applications,

dense polymer thin films are typically required, with thicknesses ranging from tens of nanometers to millimeters.[1-5] Water vapor passes through the dense film via a solution-diffusion process,[6] in which the water vapor first dissolves at the interface between the polymer and the water vapor, and then diffuses through the polymer facilitated by transient free-volume created by local polymer chain dynamics. The diffusion process can be described by Fick's law, with the diffusivity D_m as the material parameter.

Direct measurement of the diffusion of water vapor in nanoscale polymer films is challenging due to the lack of experimental tools with adequate sensitivity and temporal resolution. Dynamic absorption (e.g., gravimetric methods),[7, 8, 9] and Fourier transform infrared-attenuated total reflectance (FTIR-ATR) spectroscopy[10-12] have been used to measure the concentration-gradient-driven diffusion of water vapor in polymer films. The temporal resolution of these techniques is on the order of seconds and the thickness of the polymer sample required is therefore typically tens of microns. For a film with a thickness of 100 nm and $D_m = 1x10^{-11}$ $m^2 s^{-1}$, water vapor diffuses through the film on a time scale of 1 ms. Therefore, conventional methods cannot directly probe the kinetics of water diffusion in nanometer-scale polymer layers due to limited time resolution.

Furthermore, both dynamic absorption and FTIR-ATR typically report an average diffusivity over a period of time and large range of hydration. The average diffusivity is not a good representation of the water vapor transport process when D_m changes significantly with the hydration level of the polymer. Other less common techniques, such as pulsed field gradient nuclear magnetic resonance (NMR)[13, 14] and quasi-elastic neutron scattering (QENS)[15], can measure the self-diffusion of water vapor on short time-

scales, e.g., ~ms for NMR and ~ps for QENS. However, a relatively large sample volume is needed for these techniques due to the limitation in sensitivity.

Here we describe a laser-based pump-probe technique, frequency-domain probe beam deflection (FD-PBD) that enables measurement of water vapor diffusion in nanoscale polymer thin films with microsecond temporal resolution, micrometer spatial resolution and high sensitivity. In FD-PBD, a pump laser beam heats the sample and the deflection of a probe laser beam is used to monitor gradients of the index of refraction and the surface slope.

Previously, laser beam deflection has been applied in measurements of the thermophysical properties of materials (e.g., thermo-optic coefficient[16, 17] and thermal diffusivity[18, 19]) and diffusion of molecules,[20-22] ions[23, 24] and nanoparticles[25] in bulk liquids. By measuring the laser beam deflection in the time domain with ultrahigh time resolution, our group previously described the measurement of the coefficient of thermal expansion (CET) and elastic constants of thin films.[26, 27]

Here, we use probe beam deflection in the frequency domain (FD-PBD) to measure the diffusion of water vapor in polymer films approximately 100 nm thick. The polymer film is placed in contact with pure water vapor at a given pressure. The pump laser is modulated over a wide range of frequencies, generating an oscillating temperature excursion in the polymer film that periodically modulates the equilibrium water concentration of the film. This perturbation of equilibrium drives the diffusion of water molecules to restore the system to a new equilibrium. The probe laser detects changes in the refractive index and thickness of the polymer film caused by changes in the water content of the film. The water vapor diffusivity is determined by fitting the deflection

data to a comprehensive model of the experiment with the diffusivity as the unknown parameter.

In what follows, we first describe the model for FD-PBD, which includes thermal transport, mass transport, multilayer optics, and changes in the refractive index and thickness of the multilayer system due to the temperature field and mass concentration field. We then describe the apparatus we use for implementing FD-PBD. We apply FD-PBD to spin-coated polymer films of various compositions and thicknesses under varying water vapor pressures to validate the method and demonstrate the usefulness of FD-PBD for accurate measurements of water vapor diffusion. We finish by demonstrating the capability of FD-PBD for determining the water vapor diffusivity in nanoscale polymer membrane at different hydration levels.

II. MODEL OF BEAM DEFLECTION IN THE FREQUENCY DOMAIN

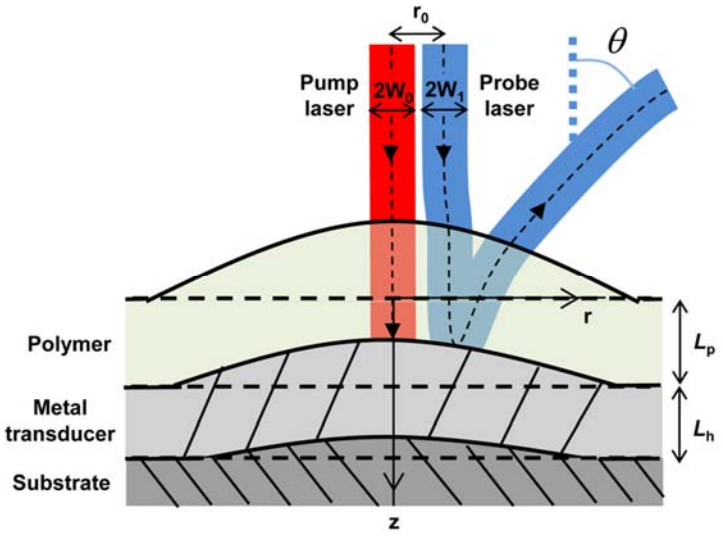

FIG. 1. Schematic illustration of the sample geometry and the detection scheme of frequency domain probe beam defection (FD-PBD). The cylindrical coordinate system uses *z* and *r* as the

two axes. The pump and probe beams are shown well-separated for clarity of the illustration. In the actual measurement, the pump beam and the probe beam are partially overlapped to maximize the deflection signal.

Figure 1 shows the sample configuration and the geometry of our experiments. The sample consists of a polymer layer (with a thickness L_p), a thin layer of metal transducer (typically Al, with a thickness L_h) and a bulk substrate (typically fused silica). The sample is surrounded by vapor (water vapor in the experiments discussed in this paper) that acts as a reservoir for the molecular species that diffuse in the polymer film. The pump beam passes through the water vapor and the polymer film, and is partially absorbed and mostly reflected by the Al film. The pump beam is modulated at angular frequency ω. The heat dissipated in the Al film generates an oscillating temperature field in the Al film and neighboring layers. The $1/e^2$ intensity radius of the focused pump beam is W_0. The oscillating temperature field in the polymer film alters the equilibrium concentration of water in the polymer and drives the exchange of water molecules between the polymer film and the surrounding vapor.

The oscillating temperature and water vapor concentration fields produce oscillating elastic strains and changes of refractive index. These effects are detected by the deflection of a probe beam with an optical path that is approximately parallel to the pump beam but displaced from the pump beam by a distance r_0. The $1/e^2$ intensity radius of the probe beam is W_1. The deflection angle of the probe beam θ is measured by a quadrant photodiode using lock-in detection at the heating frequency, i.e., the modulation frequency of the pump ω.

Beam deflection is the change of optical path created by a lateral gradient in the phase of the optical wave.[26] Several distinct mechanisms contribute to the beam

deflection: displacements of the reflecting surfaces, changes of refractive indexes and thicknesses of the materials that the optical wave passes through, and changes in the phase of Fresnel reflection coefficients at interfaces in the optical path.

To calculate the total beam deflection, we first solve the heat diffusion equation in the sample and in the water vapor above the sample. We then use the solution for the temperature field as the input to the equations that describe the diffusion of water in the polymer layer. Finally, we use the solutions for the temperature and water concentration fields as inputs to a multilayer optical model to calculate the change in the optical phase of the probe beam $\Delta\psi$. The optical model takes into account multiple reflections at the top and bottom surface of the polymer layer using a transfer matrix approach.

The calculated change in optical phase $\Delta\psi$ contains contributions from the thermal expansion and swelling of the polymer layer, the change of refractive index in the polymer layer caused by the temperature field and the water concentration field, and the changes in the phase of the Fresnel reflection coefficient at the Al/polymer interface. Any coupling among these changes in optical phase has also been captured by the multilayer optical model. Finally, we convert $\Delta\psi$ to an equivalent surface displacement Z_0 and add Z_0 to the surface displacements created by the thermal expansion of the Al layer (Z_1), the deformation of the substrate due to the stresses generated in thin films above (Z_2), the thermal expansion of the substrate (Z_3) and the equivalent surface displacement caused by the thermo-optic effect in the water vapor (Z_4). We ignore any additional couplings among Z_0 to Z_4 because they are generally quite small. The total beam deflection θ is obtained by convoluting the probe beam intensity with the lateral spatial gradient of the added equivalent surface displacements $\sum_{i=0}^{4} Z_i$.

A. Temperature distribution in the spatial and temporal frequency domain

We treat the sample and the water vapor above the sample as a layered system (Fig. 1). Each layer is labeled by an index j and has a thickness L_j. The total number of layers is N. The first layer (j = 1) is the water vapor and the last layer (j = N) is the substrate. The origin of the cylindrical coordinate lies at the bottom of the first layer; the positive z-direction is toward the substrate. Typically, we have four layers: the water vapor, the polymer thin film, the Al transducer and the fused silica substrate. However, the model can be easily extended to an arbitrary number of layers.

The sample and the pump laser beam that heats the sample are cylindrically symmetric. The heating power and temperature field oscillate at an angular frequency ω. We apply Hankel transform and Fourier transform to reduce the dimensionality of the heat diffusion equation and convert the partial differential equations to algebraic form. The temperature field is subsequently obtained by solving the heat diffusion equation via a transfer matrix method in the spatial frequency domain (k) and the temporal frequency domain (ω) (Appendix A).[26, 28] The heat source is set at the Al/polymer interface and heat flows in both the up (into the polymer and water vapor) and down (into the Al film and the silica substrate) directions. The top layer (water vapor) and the bottom layer (silica substrate) are treated as thermally thick. The temperature field T_j in each layer is

$$T_j(k,\omega,z) = \overline{T}_j^{+} \exp(u_j z) + \overline{T}_j^{-} \exp(-u_j z), \tag{1}$$

$$u_j = (\frac{i\omega}{D_j} + 4\pi^2 \mathrm{k}^2)^{1/2}, \tag{2}$$

where z stands for the coordinate in the layer j = 1 and is defined as the distance from the top surface of each layer for the rest of the layers (j = 2 to N); $\overline{T}_j^{+}$ and $\overline{T}_j^{-}$ are the

amplitudes of the thermal waves traveling backward and forward for the layer j, respectively; D_j is the thermal diffusivity of the layer j. Since the top and bottom layers are thermally thick, $\overline{T}_1^- = \overline{T}_N^+ = 0$.

B. Distribution of the change of water concentration in the polymer film

Without heating, the water content inside the polymer is at equilibrium concentration C_{eq}. We assume that a temperature rise ΔT creates an immediate change of water concentration $\frac{dC_{eq}}{dT}\Delta T$ at the top surface of the polymer film. Subsequent diffusion of water inside the polymer results in a new distribution of water concentration. These assumptions are consistent with the basic assumptions of the solution-diffusion model, and are valid if the dissolution of water vapor at the polymer/water vapor interface is much faster than the diffusion of water vapor through the polymer film.[29]

We obtain the change of water concentration C by solving the mass diffusion equation in the spatial and temporal frequency domain. Since the time-scale for heat transport in the polymer is much smaller than the time-scale of mass transport, in the solution for the change of water concentration C, we assume that the temperature field in the polymer is homogenous in the vertical direction and oscillates with an amplitude T_p. (The thermal diffusion constant of the polymer layer is on the order of 10^{-7} m^2 s^{-1} while the diffusion constants of water in polymers is typically at least two orders of magnitude smaller, $<10^{-9}$ m^2 s^{-1}.) In fact, even at the highest frequencies employed in the experiments described below, the temperature in the z-direction of the polymer layer is essentially homogenous, i.e., the polymer layer is "thermally thin" at 100 kHz.

The boundary condition for mass transport at the top surface of the polymer layer is $C\left(z=0\right)=\frac{dC_{\text{eq}}}{dT}T_p$. This boundary condition assumes no limitation in the mass transport in the vapor layer, i.e., the resistance for water vapor diffusion only exists in the polymer layer. This assumption is well-satisfied for pure water vapor (including the saturated pure water vapor and the pure water vapor at reduced pressure as used in our experiments) but would not be valid in moist air. Since no other gas molecules exist in the pure water vapor, there is no mutual diffusion in the vapor layer to limit the mass transport. At the polymer/Al interface, the boundary condition is $\frac{dC}{dz}\left(z=L_p\right)=0$ since no water vapor enters the Al film. L_{p} is the thickness of the polymer. The change of water concentration in the polymer is

$$C\left(k,\omega,z\right)=\frac{dC_{eq}}{dT}T_p\frac{\cosh(\lambda_m(L_p-\text{z}))}{\cosh(\lambda_m L_p)}, \tag{3}$$

$$\lambda_m=\sqrt{4\pi^2k^2+q_m^2}, \tag{4}$$

$$q_m=\sqrt{i\omega/D_m}\ . \tag{5}$$

C. The change in the optical phase of the probe beam calculated using the multilayer optical model

When the thickness of the polymer film approaches a significant fraction of the laser wavelength (λ), the phase of the optical wave has contributions from multiple reflections at the top and bottom surface of the polymer. To account for such effects, we calculate the difference between the optical phase (ψ) of the reflected probe beam and that of the incident probe beam using a multilayer optical model. We then obtain the

change in this optical phase ($\Delta\psi$) caused by the temperature field and the water concentration field. The multilayer optical model we adopt here is applicable to polymer films with arbitrary thicknesses and compositions.

The calculation starts by evaluating the electrical fields (E-fields) of the incoming and reflected optical waves using an optical transfer matrix method.[30, 31] The E-field in layer *j* in the spatial frequency (*k*) and optical frequency (ω_{op}) domain is

$$E_j = \overline{E}_j^{+} e^{V_j z} + \overline{E}_j^{-} e^{-V_j z}, \tag{6}$$

$$V_j = \sqrt{-(\frac{\omega_{op} n_j}{c_0})^2 + 4\pi^2 k^2}, \tag{7}$$

where $\overline{E}_j^{+}$ and $\overline{E}_j^{-}$ are the complex amplitudes of the E-fields of the optical wave traveling forward and backward in the layer *j*, respectively, c_0 is the speed of light and n_j is the refractive index of layer *j*. The boundary conditions require the continuity of the electrical and magnetic fields at each interface. This allows the calculation of the amplitudes of E-fields in each layer:

$$\begin{pmatrix} \overline{E}_{j-1}^{+} \\ \overline{E}_{j-1}^{-} \end{pmatrix} = \frac{1}{2V_{j-1}} \begin{pmatrix} e^{-V_{j-1}L_{j-1}} & 0 \\ 0 & e^{V_{j-1}L_{j-1}} \end{pmatrix} \begin{pmatrix} V_{j-1}+V_j & V_{j-1}-V_j \\ V_{j-1}-V_j & V_{j-1}+V_j \end{pmatrix} \begin{pmatrix} \overline{E}_j^{+} \\ \overline{E}_j^{-} \end{pmatrix}, \tag{8}$$

for j =*h* to 3 and

$$\begin{pmatrix} \overline{E}_1^{+} \\ \overline{E}_1^{-} \end{pmatrix} = \frac{1}{2V_1} \begin{pmatrix} V_1+V_2 & V_1-V_2 \\ V_1-V_2 & V_1+V_2 \end{pmatrix} \begin{pmatrix} \overline{E}_2^{+} \\ \overline{E}_2^{-} \end{pmatrix}. \tag{9}$$

The matrix multiplication starts from the Al layer (layer *h*) because the Al layer is optically opaque in the experiment (i.e., the penetration depth of the laser is much smaller than the thickness of the Al layer). $\overline{E}_h^{-} = 0$ due to the absence of any optical wave that

travels backward in the Al layer. The complex reflectivity r_{ref} is the ratio of the E-field of the reflected wave to that of the incoming wave at the top surface of the sample. At temperature T_0,

$$r_{\text{ref}}(T_0) = \overline{E}_1^{-}(T_0) / \overline{E}_1^{+}(T_0) \tag{10}$$

and the phase of $r_{\text{ref}}(T_0)$ is a real number $\psi(T_0)$.

In response to a change of temperature (T_p) and the associated change of water concentration (C) in the polymer, the phase of the complex reflectivity $\psi(T_0+T_p)$ is altered by multiple factors: changes in the refractive indexes of the Al and the polymer layers as a function of temperature, the change in the refractive index of the polymer as a function of water concentration field, and the change in the thickness of the polymer as a function of temperature and water concentration.

To obtain the change in ψ created by the oscillations in temperature (i.e., $\Delta\psi = \psi(T_0+T_p) - \psi(T_0)$), we calculate the complex reflectivity $r_{\text{ref}}(T_0 + T_p)$ by the same transfer matrix method with the changed refractive indexes and thicknesses of materials in the temperature and concentration fields. To facilitate using the transfer matrix method, we further discretize C in the z direction in consideration of the large vertical gradient of water concentration in the polymer. This is achieved by dividing the polymer layer into multiple layers with the thickness of each layer (L_d) much smaller than the water diffusion length $\sqrt{D_m / \omega}$. A new layer system forms as a result of the discretization, with the number of each layer marked by j', where the first layer j'=1 is the water vapor, j'= 2 to L_p/L_d +1 correspond to the divided polymer layers and j'=L_p/L_d+2 is the Al layer. In

the new layered system, the water concentration field and the changes in the refractive indexes and the thicknesses of each layer adopt the form

$$C_{j'}\left(z,k,\omega\right)=\frac{dC_{\text{eq}}}{dT}T_p\frac{\cosh(\lambda_m(L_p-(j'-2)L_d))}{\cosh(\lambda_m L_p)}, \tag{11}$$

$$\Delta n_{j'}(T_p)=\frac{dn_{j'}}{dT}T_p+\frac{dn_{j'}}{dC_{\text{eq}}}C_{j'}, \tag{12}$$

$$\Delta L_{j'}(T_p)=\alpha_{T,j'}L_{j'}\frac{1+v_{j'}}{1-v_{j'}}T_p+\alpha_{m,j'}L_{j'}\frac{1+v_{j'}}{1-v_{j'}}C_{j'}, \tag{13}$$

for all the polymer layers (i.e. j'= 2 to L_p/L_d +1), and

$$\Delta n_{j'}(T_p)=\frac{dn_{j'}}{dT}T_p \tag{14}$$

for the water vapor (j'= 1) and the Al layer (j'= L_p/L_d+2), where $\frac{dn_{j'}}{dT}$ is the thermo-optic coefficient, $\alpha_{T,j'}$ is the coefficient of thermal expansion, $\frac{dn_{j'}}{dC_{\text{eq}}}$ is derivative of the refractive index to the water concentration, $\alpha_{m,j'}=\frac{1}{L_{j'}}\frac{dL_{j'}}{dC_{\text{eq}}}$ is the coefficient of expansion due to the water concentration field, and $v_{j'}$ is the Poisson's ratio for the layer j'.

Although $\Delta n_{j'}(T_p)$ and $\Delta L_{j'}(T_p)$ oscillate at the heating frequency, we treat them as constants during the application of the transfer matrix method to get $r_{ref}(T_0+T_p)$ in the optical frequency domain. This is valid since the optical frequency (ω_{op}) is much higher than the heating frequency (ω). To calculate the real and imaginary parts of $\Delta\psi$ (T_p) (i.e., the optical response that is in-phase and out-of-phase with the heating frequency), we

only need to apply the optical transfer matrix twice. The first calculation uses the real part of the temperature T_p and the real part of the water concentration C to determine $\Delta n_j(T_p)$ and $\Delta L_j(T_p)$ via Eq. (12), Eq. (13) and Eq. (14). These values for the changes in optical index and layer thickness are then used as inputs to the optical model. The output of the optical model is the added phase of the reflected wave, a real number that corresponds to the real part of $\Delta\psi$ (T_p). Similarly, adopting the imaginary parts of T_p and C in the calculation results in the imaginary part of $\Delta\psi$ (T_p).

To facilitate comparisons with other mechanisms that contribute to the probe beam deflection, we convert the change of phase of the optical waves to an equivalent surface displacement

$$Z_0(k,\omega) = -\Delta\psi \frac{\lambda}{4\pi}. \tag{15}$$

Strictly, Z_0 should be multiplied by a factor of n_1/n_{air} (the refractive index of air) to account for the refraction of the probe beam when passing from the water vapor to ambient air (where the detector is placed). However, we ignore this factor here and in the following discussion because n_1/n_{air} is close to unity. We define the surface displacement as positive if the effect of the corresponding mechanism reduces the optical path of probe beam.

D. Contributions from deformation of the metal transducer and the substrate, and the thermo-optic effect in the water vapor

The probe beam deflection also contains contributions from the thermal expansion of the Al (Z_1), the elastic deformation of the substrate created by the stresses in the Al and

polymer layers (Z_2), the thermal expansion of the substrate (Z_3) and the thermo-optic effect in the water vapor (Z_4). The induced equivalent surface displacements from Z_1 to Z_4 have been discussed previously in ref. 26 and ref.27.[26, 27] Here we reproduce those results and apply them to our case for completeness.

Z_1 is the effective vertical thermal expansion of the metal transducer layer (i.e. Al).

$$Z_1 = \frac{1+v_h}{1-v_h}\alpha_{T,h}\int_0^{L_h} T_h dz \approx \frac{1+v_h}{1-v_h}\alpha_{T,h} T_p L_h , \qquad (16)$$

where h denotes the number of the Al layer, v_h is the Poisson's ratio, $\alpha_{T,\mathrm{h}}$ is the coefficient of thermal expansion (CET) and L_h is the thickness. $T_h \approx T_p$ within the frequency range of the measurements that are described below (up to 100 kHz). Z_1 is positive since it reduces the optical path of the probe beam.

Z_2 is the elastic deformation of the substrate created by the inhomogeneous shear stress generated in all the thin films above. Within the frequency range that we are interested in (i.e. <100kHz),

$$Z_2 = \frac{\upsilon_T^2}{\upsilon_L^2 - \upsilon_T^2}\frac{1+v_N}{Y_N} g , \qquad (17)$$

$$g = \sum_{j=2}^{N-1}\left(\frac{Y_j}{1-v_j}\alpha_{T,j}\int_0^{L_j} T_j dz\right) + \frac{Y_p}{1-v_p}\alpha_{m,p}\int_0^{L_p} C dz , \qquad (18)$$

where Y_j is the Young's modulus of the layer j; g is the plane stress in the thin films created by the thermal expansion of the films and the lateral constraints of the substrate; the subscript p stands for the number of the polymer layer; $\alpha_{\mathrm{m},p}$ is the coefficient of expansion due to the change of water concentration in the polymer layer (defined

previously); and υ_L and υ_T are the speeds of the longitudinal and transverse acoustic waves in the substrate, respectively.

Z_3 is the thermal expansion of the substrate in the vertical direction. At low frequency,

$$Z_3 = \frac{1+\nu_N}{1-\nu_N}\alpha_{T,N}\frac{u_N}{q_N^2}(1-\frac{2\pi k}{u_N})\frac{\upsilon_L^2}{\upsilon_L^2-\upsilon_T^2}\overline{T}_N^-, \quad (19)$$

$$q_N^2 = \frac{i\omega}{D_N}. \quad (20)$$

Z_4 originates from the thermo-optic effect in the water vapor and can be expressed as

$$Z_4 = -\frac{1}{u_1}\frac{dn_1}{dT}T_1(z=0). \quad (21)$$

The total beam deflection depends on the sum of each effective surface displacement from Eqs. (15), (16), (17), (19), (21),

$$Z = \sum_{i=0}^{4} Z_i. \quad (22)$$

E. Conversion from surface displacements to probe beam deflection

We follow the previous treatment to convert the equivalent surface displacement (Z) to the measured deflection of the probe beam (θ).[26, 27] In the approximation of geometric optics, the beam deflection at any location is just twice the lateral gradient of the real space surface displacement. Convolution of the probe intensity with the radial derivative of the surface displacement at r_0 (i.e. the separation between the pump and probe beam) results in

$$\theta = 8\pi^2\int_0^\infty Z\exp(-\pi^2k^2W_1^2/2)J_1(2\pi kr_0)k^2dk, \quad (23)$$

where W_1 is the $1/e^2$ spot size of the probe beam and J_1 is the Bessel function of the first kind.

F. The magnitude and characteristic frequency of beam deflections originating from each mechanism

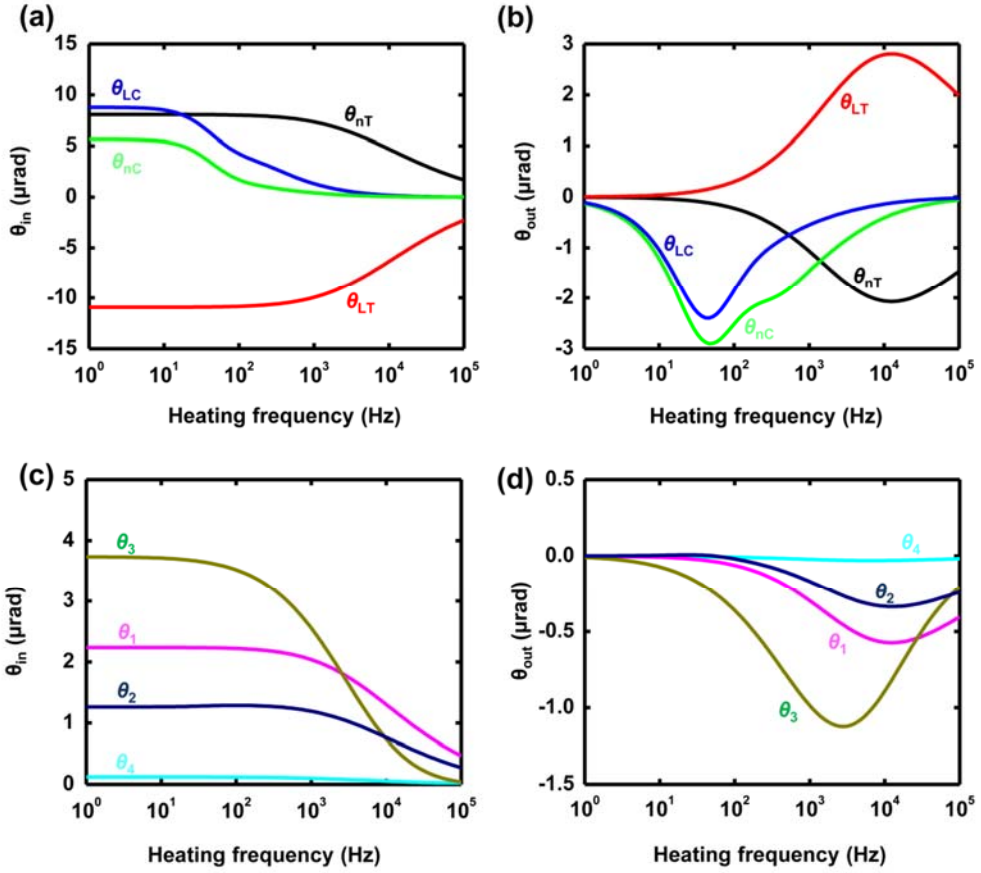

FIG. 2. (a)-(b) Calculated in-phase (a) and out-of-phase (b) components of the deflection angles caused by the changes in the refractive indexes of the sample due to the temperature field (θ_{nT}), by the change in the thickness of the polymer due to the temperature field (θ_{LT}), by the change of the refractive index in the polymer due to the water concentration field (θ_{nC}) and by the change in the thickness of the polymer due to the water concentration field (θ_{LC}). (c)-(d) Calculated in-

phase (c) and out-of-phase (d) components of the deflection angles caused by the thermal expansion of Al (θ_1), by the deformation of the substrate due to stresses in the thin films (θ_2), by the thermal expansion of the substrate (θ_3) and by the thermo-optic effect in the water vapor (θ_4).

Figure 2 shows the calculated in-phase and out-of-phase components of the deflection angles by each of the aforementioned mechanisms as a function of heating frequency. We emphasize the out-of-phase components in Fig. 2 because they reveal both the magnitude and the characteristic frequency of the beam deflection from each mechanism. The layered sample structure used in the simulation is water vapor / poly (methyl methacrylate) PMMA (100 nm) / Al (80nm) / a-SiO_2 (amorphous silica). Input parameters to the model include the amplitude of the heating power absorbed by the Al transducer ≈ 0.9 mW, which is estimated by taking into account of the input pump laser power, the absorption of Al (calculated via multilayer optics) and the transmission of the optical window and objective lens used in the experiments. Other geometric parameters are $W_1 = W_0 = 11.3$ μm and $r_0 = 12$ μm. Important materials properties implemented in the modeling are $D_m = 1.1\times10^{-12}$ m^2 s^{-1}, $\frac{dn_p}{dC_{eq}}\frac{dC_{eq}}{dT} = -1.0\times10^{-4}\,K^{-1}$, $\alpha_{m,p}\frac{dC_{eq}}{dT} = -2\times10^{-5}\,K^{-1}$, $\alpha_{T,p} = 33\times10^{-6}\,K^{-1}$ and $\frac{dn_p}{dT} = -1.1\times10^{-4}\,K^{-1}$. The values used here are derived from experiments described below. Additional material properties are listed in Table 1 in Appendix B. Details of the calculation appear in Appendix C.

Although all mechanisms described previously contribute to beam deflections, the components that are relevant to measuring the mass diffusion constant originate from changes in the refractive index and in the thickness of the polymer due to the water

concentration field. Such components of beam deflections are denoted as θ_{nC} and θ_{LC}. The values are plotted in Fig. 2(a)-(b). The magnitude of θ_{nC} correlates positively with $\frac{dn_p}{dC_{\mathrm{eq}}}\frac{dC_{\mathrm{eq}}}{dT}$ and the thickness of the polymer (L_{p}). Likewise, the magnitude of θ_{LC} mainly depends on $\alpha_{\mathrm{m},p}\frac{dC_{\mathrm{eq}}}{dT}$ and L_{p}. Both θ_{nC} and θ_{LC} follow a time-scale of mass diffusion in the polymer layer. As shown in Fig.2 (b), the minimum of the out-of-phase signal in θ_{nC} and θ_{LC} appear at a frequency (f_{C}) roughly corresponding to the reciprocal of the mass diffusion time in the polymer layer $\frac{D_m}{\pi L_p^2}$ (≈ 35 Hz).

Figure 2(a)-(b) also show the in-phase and out-of-phase components of the deflection angles directly induced by the temperature field in the polymer film. θ_{LT} is caused by the thermal expansion of the polymer and θ_{nT} represents the beam deflection caused by the thermo-optic effects in the sample. θ_{LT} and θ_{nT} are comparable in magnitude but show opposite signs because the thermal expansion increases the optical path while the thermo-optic effect reduces the optical path. On the other hand, both θ_{LT} and θ_{nT} vary in a characteristic time-scale of heat diffusion that is mainly controlled by the laser spot size (W_0) and the thermal diffusivity of the a-SiO_2 substrate (D_N); i.e., the frequencies of the maximum of the out-of-phase of θ_{LT} and that of the minimum of θ_{nT} (f_{T}) scale with $\frac{D_N}{W_0^2}$ (≈ 6 kHz).

Figure 2(c)-(d) shows the in-phase and out-of-phase components of the contribution to the deflection angles coming from Z_1 to Z_4, respectively. The largest

contribution comes from the thermal expansion of the substrate θ_3. Even though the coefficient of thermal expansion of amorphous silica is small, the depth of the silica substrate that contributes to the thermal expansion signal is large, on the order of W_0. The contribution of the water vapor θ_4 is insignificant due to the negligible thermo-optic coefficient of the water vapor even at saturated vapor pressure (0.38 psi at 22 ^oC). Deflection angles caused by the thermal expansion of the Al (θ_1) and by the stress induced deformation of the substrate (θ_2) follow the time scale of heat diffusion in the substrate across the length scale of W_0. The minimum of θ_3 appears at a lower frequency compared with θ_1 and θ_2 due to the heat spreading inside the substrate layer; i.e., Z_1 and Z_2 depends only on the surface temperature of the sample while Z_3 depends on the integration of the temperature field over a depth of W_0.

Overall, the time scale of mass diffusion is $\frac{L_p^2}{D_m}$ and the time scale for heat diffusion contributing to the beam deflection is $\frac{W_0^2}{D_N}$. The detection of the mass transport is largely simplified by separating the characteristic time scales of heat and mass diffusion with appropriate choices of experimental parameters. Practically, we make sure $\frac{W_0^2}{L_p^2} << \frac{D_N}{D_m}$ in our experiments described below. In this case, the frequency corresponding to the minimum out-of-phase signals caused by mass diffusion (f_C) is significantly lower than that corresponding to the minimum out-of-phase signals directly originating from heat diffusion (f_T). In principle, however, if the polymer is thin enough and the mass

diffusion constant is high enough, $\frac{W_0^2}{L_p^2} >> \frac{D_N}{D_m}$ is also a possible scenario for the measurement of mass diffusion.

III. IMPLEMENTATION OF FD-PBD

A. Sample preparation and characterization

We prepare thin polymer films by spin-coating polymer solutions on substrates followed by baking on a hot plate. The substrates are polished fused silica (0.5 mm thick, University Wafer) coated by a thin layer of Al (≈ 80 nm) deposited by magnetron sputtering. The selection of fused silica (i.e., a-SiO_2) as the substrate reduces the background deflection signals created by the thermal expansion of the substrate (α_T of fused silica ≈ 0.5×10^{-6} K^{-1}).[32] The solutions of poly (methyl methacrylate) (PMMA) are either used as-received (495PMMA A5, A4, A2, MicroChem) or diluted by adding anisole (anisole: 495PMMA A2 = 1:1 in volume). We prepare cellulose acetate (CA) solutions by dissolving CA (powder, 39.8 wt. % acetyl, M_n = 30 kg mol^{-1}, Sigma-Aldrich) in acetone at various concentrations (10 mg mL^{-1} to 20 mg mL^{-1}). Poly-(vinylpyrrolidone) (PVP, M_w = 25 kg mol^{-1}, Sigma-Aldrich) is dissolved in dimethylformamide (DMF) to form the corresponding solution (60 mg mL^{-1}). We dilute the as-received polyimide (PI 2545, HD microsystem) by adding about 70% N-methyl-2-pyrrolidone (NMP). Spin-coating of the various solutions with speeds ranging between 1000 and 4000 rpm results in thin films of thicknesses between 25 nm and 350 nm. After spin-coating, baking the sample at 150 °C for 5 min removes the remaining solvent. The PI film is further cured in an oven at 250 °C for 2 hours.

The polyamide membrane was synthesized via interfacial polymerization of piperazine (PIP, 99% pure, Sigma Aldrich) and trimesoyl chloride (TMC, 98% pure, Sigma Aldrich) using a support-free approach.[33] Briefly, addition of 20 ml PIP solution (0.01 wt% in water) to a petridish, followed by dropwise addition of 15 ml TMC (0.005 wt% in hexane) to the surface of the aqueous PIP solution initiates the interfacial polymerization at the water/hexane interface. After 5 minutes, both the excess aqueous and organic solutions are removed from the petridish by pipette. The PIP/TMC membrane is repeatedly rinsed by hexane on the top surface and by water on the bottom surface. Finally, the membrane is floated on 20 mL of water to facilitate transfer to the substrate by sliding the Al/a-SiO_2 substrate underneath and subsequently draining the water via pipette.

The thicknesses of PMMA, CA, PVP, PI and PIP/TMC films were measured by spectroscopic ellipsometry (VASE, J.A.Woollam) under ambient condition. We further verified the thicknesses of the CA and PIP/TMC films by using atomic force microscopy (AFM). Scratching a portion of the polymers off the substrate by a razor blade forms a step edge, which allows the access of the thicknesses by AFM. We found that the thicknesses of the films measured by AFM matched with the thicknesses obtained by ellipsometry within the experimental uncertainties of 10 nm. The surface roughness of the films is smaller than 8 nm as verified by scanning multiple areas of 10 μm x 10 μm using AFM. We obtained the thicknesses of the Al transducers using picosecond acoustics.[34] The hydration of PIP/TMC films was measured by quartz crystal microbalance. The areal density of the dry film was determined by transferring the film to a chrome/gold 5 MHz sensor (Stanford Research Systems), drying the film in an oven at

100 °C for 20 min, and then heating the film to 200 °C for 4 min to drive off water prior to measurement. The dry mass of the film was measured under a nitrogen atmosphere. The dry polymer coated sensor was then transferred to a Ziplock bag with a small beaker containing either a saturated solution of $CaCl_2$ in water or pure water to produce 40% and 100% relative humidity, respectively. The mass change of the sensor was measured after 24 hours of incubation to determine water sorption.

B. Experimental apparatus

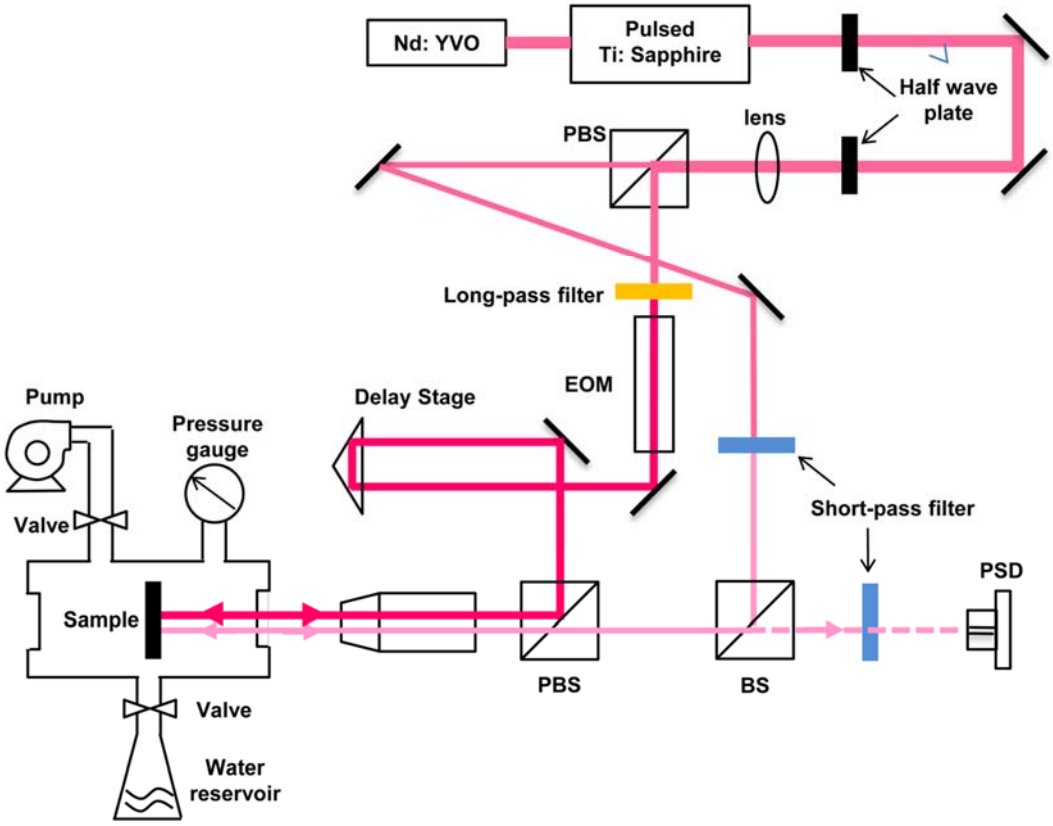

FIG. 3. Schematic diagram of the experimental apparatus for using FD-PBD to measure the diffusivity of water vapor in polymer thin films.

Figure 3 shows a schematic diagram of the experimental setup for FD-PBD. The setup is a modification of the two-tint time domain thermoreflectance (TDTR) system.[28, 35] Briefly, a Ti:sapphire laser generates pulse trains (wavelength ≈ 783 nm, full width of half maximum ≈ 10 nm) that are physically separated by a polarized beam splitter (PBS) to form pump and probe beams. A long-pass filter (onset of cut-off at 790 nm) and a short-pass filter (onset of cut-off at 780 nm) further separate the pump and the probe laser spectrally. The pump laser passes through an electro-optic modulator (EOM) operating at the frequency (*f*) before the beam enters a delay stage that changes the optical path. An objective lens with a focal length *F* focuses both pump and probe lasers on the sample surface and collimates the reflected probe beam. The reflected pump beam is blocked from entering the detector by the PBS and a sharp-edge short-pass filter (onset of cut-off at 780 nm).

The major changes from the TDTR system to the FD-PBD setup are 1) removing the second lens that is used in TDTR to focus the reflected probe beam on the detector and 2) replacing the photodetector with a position sensitive detector (PSD, New Focus quadcell photoreceiver model 290X, cut-off at 100 kHz). During FD-PBD measurements, we fix the delay stage at a position where the probe pulses arrive at the sample 50 ps before the arrival of the pump pulses. Scanning the EOM frequency *f* from 10 Hz to 20 kHz covers the frequency range of water diffusion in the films we studied. We use an audio-frequency (AF) lock-in amplifier (Stanford Research SR 830) to detect the deflection signals from the PSD at frequency *f*. FD-PBD can also be implemented in a manner similar to the design used for frequency-domain thermoreflectance (FDTR) which uses continuous-wave (CW) lasers.[36] In our experience, the short coherence length

of mode-locked lasers is an advantage over the much longer coherence length of CW lasers because the short-coherence length suppresses interference effects in the signals.

The sample is placed in a customized chamber with an optical window (fused silica, thickness ≈ 1 mm) to admit the pump and probe laser beams (Fig. 3). A mechanical pump evacuates the chamber. A controlled amount of water vapor can be introduced into the chamber by closing the value between the chamber and the pump, and opening the valve that leads to a water reservoir. We monitor the chamber pressure with a piezoresistive transducer (PX409-015AV, Omega).

During measurements, the center of the PSD is first set to align with the reflected probe beam to maximize the sensitivity of the PSD. For such purpose, we chop the probe beam at a frequency of 200 Hz and minimize the differential signals in the X and Y directions in response to the modulated probe beam. When the pump beam overlaps with the probe beam, there is no deflection signal due to symmetry. We then steered the pump beam away horizontally by rotating the PBS with a differential micrometer and a high precision optical mount. We determined by both modeling and experiment that a separation (r_0) of the pump and probe beam of approximately 1.2 times of the $1/e^2$ radius (W_0) yields maximum deflection signals. With the 5× and 20× objective lens, the laser spot size W_0 were measured by TDTR beam off-set measurements[37] as 11.3 μm and 2.7 μm, respectively. Therefore, we used r_0 =12 μm and r_0 = 4 μm for the 5× and 20× lens, respectively.

We set the ratio between the average pump power and the probe power at 1:2 to maximize the signal under the same steady-state heating temperature (ΔT_{SSH}). For the 5× objective lens, a pump power of 1.5 mW and a probe power of 3 mW result in $\Delta T_{SSH} \approx$

6.5 K to 13 K (depending on the polymer type and thickness on top of the Al). For the 20× lens, a pump power of 1 mW and a probe power of 2 mW cause $\Delta T_{SSH} \approx 7$ K to 14 K. The power was measured at the back-focal-plane of the objective lens. When calculating the ΔT_{SSH}, we considered the transmission of the objective lens (0.9 for 5× and 0.7 for 20×) and the optical window (0.9), and the absorption of the Al transducer (0.13 to 0.26 depending on the thickness and type of the polymer on top of the Al layer).

C. Data processing and analysis of noise

The modulated deflection of the reflected probe beam (θ) causes a displacement of the laser spot ($x = F\theta$, F is 40 mm for 5× lens and 10 mm for 20× lens) on the PSD, which generates a differential voltage output from the PSD

$$V = \frac{x}{W}\frac{G}{0.65}V_{sum}, \tag{24}$$

where W is the free-space laser spot size, G is the second-stage gain of the PSD, V_{sum} is the total voltage output from four quadrants and the factor 0.65 comes from the calibration. The in-phase and out-of-phase data measured by the lock-in amplifier is the root-mean-square (rms) voltage

$$V_{lock-in} = \frac{F\theta}{\sqrt{2}W}\frac{G}{0.65}V_{sum} \tag{25}$$

The data have to be calibrated to account for the frequency-dependent amplitude variation and phase shifts originating from the detector and the different optical paths between the pump and probe beams.[36] To perform this calibration, we removed the short-pass filter before the PSD to leak some pump light to the PSD and recorded the amplitude and phase of the response as a function of f. The calibration curves are shown in the Appendix D. Over the frequency range of 10 Hz to 20 kHz, the amplitude of the

calibration curve is approximately constant. The phase shifts increase significantly after 1 kHz and reach about 20 degrees at 20 kHz. Such shifts mainly come from the cut off of the detector rather than the optical path, as 1 m difference in optical path only causes a phase shift of 0.02 degree at 20 kHz. We applied the calibrations to all measurements.

FD-PBD is a highly sensitive measurement due to the differential detection of the PSD and the narrow bandwidth of the lock-in amplifier. Laser power in the level of milliwatt ensures that the noise of the measurement is dominated by the pointing instability of the laser beam. Under our experimental conditions, the noise floor in terms of the deflection angle θ at 10 Hz and at >1 kHz is approximately 2x10^{-6} rad/$\sqrt{Hz}$ and 1x10^{-8} rad/$\sqrt{Hz}$, respectively.

D. Data fitting and relevant parameters

For the data obtained in vacuum where mass diffusion is negligible, the modeling curves are direct calculations with all parameters either from literature or measured independently (Appendix C). At finite water vapor pressure where mass diffusion is significant, the fit between the model and the data has three free parameters: $\frac{dn_p}{dC_{\mathrm{eq}}}\frac{dC_{\mathrm{eq}}}{dT}$, $\alpha_{\mathrm{m},p}\frac{dC_{\mathrm{eq}}}{dT}$ and D_{m}. Here, $\frac{dn_p}{dC_{\mathrm{eq}}}\frac{dC_{\mathrm{eq}}}{dT}$ and $\alpha_{\mathrm{m},p}\frac{dC_{\mathrm{eq}}}{dT}$ are pre-factors that determine the magnitude of the in-phase and out-of-phase signals. Although the contribution to the signals from the change of refractive index (corresponding to $\frac{dn_p}{dC_{\mathrm{eq}}}\frac{dC_{\mathrm{eq}}}{dT}$) has a slightly different frequency dependence compared with the contribution coming from the change of polymer thickness (corresponding to $\alpha_{\mathrm{m},p}\frac{dC_{\mathrm{eq}}}{dT}$) (Fig. 2(b)), the measurement and

model do not have enough sensitivity to quantitatively separate the two factors. In other words, the optical phase change caused by $\frac{dn_p}{dC_{\text{eq}}}\frac{dC_{\text{eq}}}{dT}$ is similar to that caused by $n_P\frac{1+\upsilon_P}{1-\upsilon_P}\alpha_{\text{m},p}\frac{dC_{\text{eq}}}{dT}$. Hence, we can only determine $\frac{dn_p}{dC_{\text{eq}}}\frac{dC_{\text{eq}}}{dT}$ and $\alpha_{\text{m},p}\frac{dC_{\text{eq}}}{dT}$ qualitatively.

In contrast, D_{m} determines the frequency (f_{C}) that corresponds to the minimum of the out-of-phase data. The extracted D_{m} has significantly smaller uncertainty than the extracted $\frac{dn_p}{dC_{\text{eq}}}\frac{dC_{\text{eq}}}{dT}$ and $\alpha_{\text{m},p}\frac{dC_{\text{eq}}}{dT}$ since the frequency position f_{C} is mainly dictated by D_{m} and the thickness of the polymer. On the other hand, the magnitude of the signal is dependent upon a large number of parameters including the material properties, sample geometries and instrument calibrations.

E. Measurement uncertainty

Uncertainties for the measured D_{m} include both experimental errors and systematic errors. The overall uncertainty is calculated by adding each source of uncertainty in quadrature. The experimental error is quantified by the goodness-of-fit[34] between the data and the model in determining f_{C} (< 5%). The systematic error can be estimated by the propagation of uncertainties in the values of the relevant parameters used in the beam deflection model, i.e. W_0, W_1, r_0 and L_p.

The sensitivity of f_{C} regarding W_0, W_1, r_0 and L_{p} appears in Appendix E.

The thickness of the polymer (L_p) is the largest source of uncertainty. For hydrophobic polymers such as PMMA and PI, L_p is, to good approximation, independent of water vapor pressure. The measurement error for L_p is <3%, which results in an overall

uncertainty for D_m of 8%. In contrast, the hydration level in CA (≈ 14 wt% at 98% relative humidity (RH)),[38] PVP (≈ 25 wt% at 80% RH)[10] and PIP/TMC (measured as ≈ 7 wt% at 40% RH and ≈ 16 wt% at 100% RH) films is high. The water vapor could swell the polymer film and change the thickness. Therefore, a relatively large error may appear when using the L_p measured under ambient condition (≈ 50% RH at 22 °C) to represent the actual polymer thickness under a vapor pressure approaching 100% RH. For instance, we estimate an uncertainty of 15% for L_p of PVP and the overall uncertainty for D_m is then ≈30%.

IV. VALIDATION OF THE FD-PBD APPROACH AND MEASUREMENTS OF WATER VAPOR DIFFUSIVITY IN POLYMER THIN FILMS

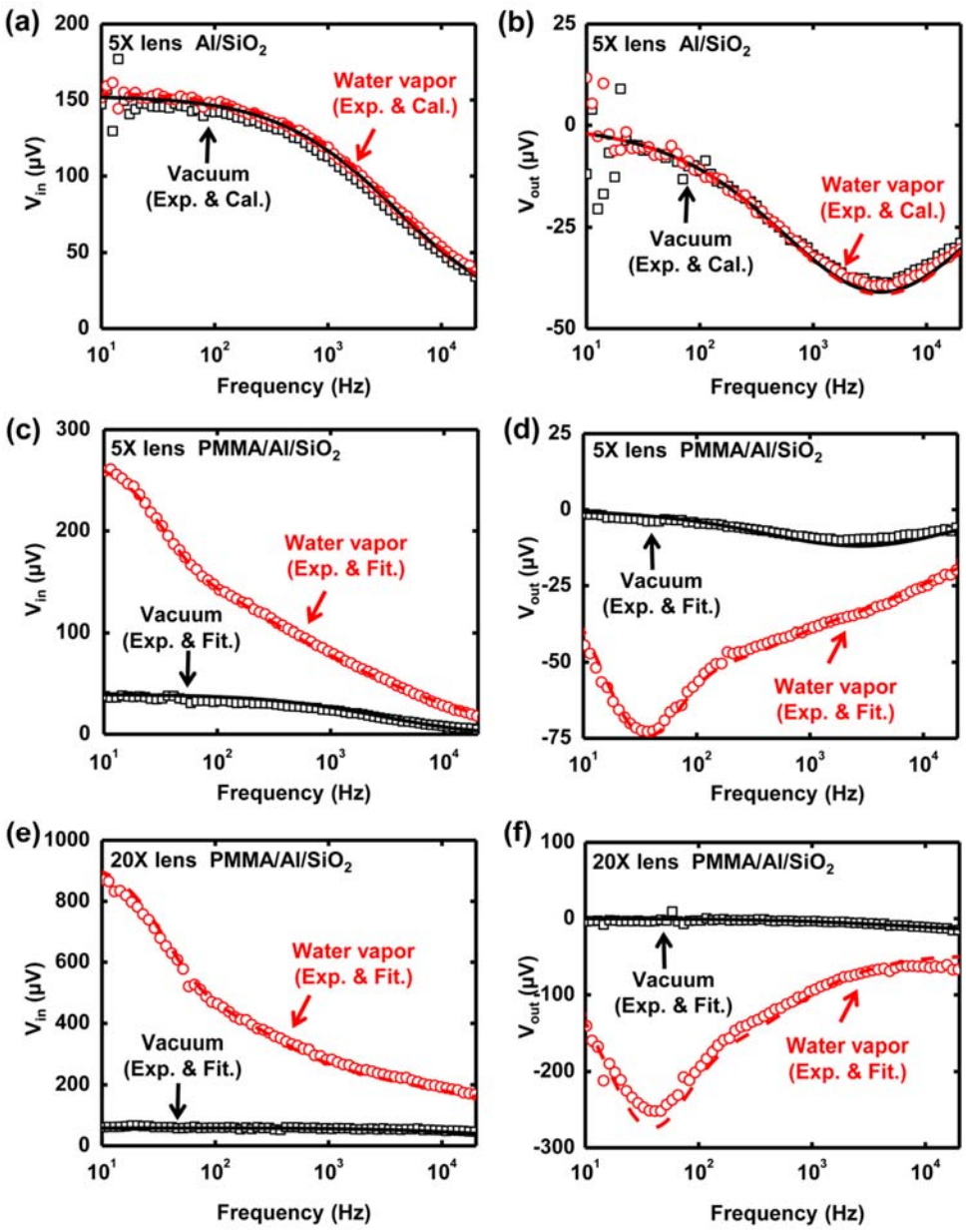

FIG. 4. (a)-(b) Measured (open symbols) and modeled (lines) in-phase data (a) and out-of-phase data (b) by FD-PBD with a 5× objective lens on a sample of Al (71 nm)/a-SiO_2. (c)-(d) Measured (open symbols) and simulated (lines) in-phase data (c) and out-of-phase data (d) by FD-PBD with a 5× objective lens on a sample of PMMA(114 nm)/Al (78 nm)/a-SiO_2. (e)-(f) Measured (open symbols) and simulated (lines) in-phase data (e) and out-of-phase data (f) by FD-PBD on the same sample with a 20× objective lens. For all the graphs, the open black squares and the

black lines are measured data and simulated signals in vacuum, respectively. The open red circles and the red dashed lines correspond to measurements and simulations under saturated water vapor (0.38 psi).

To validate the FD-PBD approach and our model for the experiment, we first applied FD-PBD to Al/a-SiO_2 and PMMA/Al/a-SiO_2 samples in vacuum and in saturated water vapor. Figure 4(a)-(b) show the V_{in} and V_{out} components of the deflection signals (symbols) measured on the Al (71 nm)/a-SiO_2 sample with a 5× objective lens. The pump power is 3 mW and the probe power is 6 mW, generating an average steady-state temperature increase of 13 K. The signals are almost identical in vacuum and in saturated water vapor. The V_{in} increases monotonically as the heating frequency decreases and gradually plateaus at low frequency. By contrast, V_{out} decreases as the heating frequency decreases from 20 kHz to ≈ 4 kHz and rises as the heating frequency is further reduced. This creates a concave shape in V_{out} on the frequency axis, with the minimum V_{out} at a frequency (f_T) that roughly corresponds to $\frac{D_N}{W_0^2}$. We calculated V_{in} and V_{out} using the deflection model (curves) with the thickness of the polymer being set as zero (other parameters used in the model are listed in Appendix B). The calculations match well with the measurements.

Figure 4(c)-(d) depict the V_{in} and V_{out} components of the deflection signals (symbols) measured on the PMMA (114 nm)/Al (78 nm)/a-SiO_2 sample with a 5× objective lens. When the sample is in vacuum, V_{in} and V_{out} as a function of the heating frequency (black rectangles) behave similarly to the data collected on the Al/a-SiO_2 sample. We fit V_{in} and V_{out} simultaneously using the thermo-optic coefficient of PMMA (dn_{PMMA}/dT) as the only free parameter (solid black lines). The best fit yields

dn_{PMMA}/dT= -0.83x10^{-4} K^{-1}, which is consistent with the literature value.[39, 40] After the water vapor enters the sample chamber and reaches the saturation water vapor pressure (0.38 psi), the magnitudes of V_{in} and V_{out} increase significantly (red circles in Fig.4 (c)-(d)). Meanwhile, an additional concave section is generated in the V_{out} curve at $f_C \approx \frac{D_m}{\pi L_p^2}$ corresponding to the rate at which water vapor diffuses through the polymer film. A kink also appears in V_{in} at the same frequency f_C. These changes in the deflection signals originate from the changes in the refractive index of PMMA and the thickness of the PMMA due to the diffusion of water vapor in the PMMA layer.

We fit the frequency position of the concave in V_{out} (also the kink in V_{in}) using D_m as the only free parameter. Subsequent fitting used $(\frac{dn}{dT})_m$ and $\alpha_{m,p}\frac{dC_{eq}}{dT}$ as free parameters to match the magnitude of V_{in} and V_{out} near the concave frequency for mass diffusion (f_C). We also noticed that the magnitudes of V_{in} and V_{out} near the heating frequency ($f_T \approx \frac{D_N}{W_0^2}$) changed slightly after the introduction of water vapor. We thereby adjusted dn_{PMMA}/dT to match with the magnitude of V_{in} and V_{out} near f_T. The overall fitting yields D_m = 1.1 x 10^{-12} m^2 s^{-1} and dn_{PMMA}/dT = -1.1 x 10^{-4} K^{-1}. The value of D_m matches well with the literature value of water vapor diffusivity in PMMA.[10, 41, 42] We used $(\frac{dn}{dT})_m = -1\times10^{-4}\,\mathrm{K}^{-1}$ and $\alpha_{m,p}\frac{dC_{eq}}{dT} = -2\times10^{-5}\,\mathrm{K}^{-1}$ to get a good match between the calculation and the experiment.

The success in the measurement of D_m relies on the effective separation between the characteristic frequency for mass diffusion (f_C) and the characteristic frequency for

heat diffusion (f_T). To further validate this approach, we applied FD-PBD to the same PMMA/Al/a-SiO_2 sample but with a 20X objective lens. The pump power is 1 mW and the probe power is 2 mW, generating an average steady-state temperature increase of about 14K. Since the laser spot size W_0 becomes smaller (from 11.3 μm for the 5× lens to 2.7 μm for the 20× lens), the concave section of the V_{out} curve that corresponds to heat diffusion moves to a higher frequency. In fact, f_T is higher than the maximum frequency in our measurements, as shown by the deflection data obtained from the sample placed in vacuum (black rectangles in Fig. 4(f)). In contrast, the frequency position of the concave part of the curve (f_C) that corresponds to mass diffusion is approximately independent of the laser spot size, as shown by the red dots in Fig. 4(f) (obtained when the sample is placed in water vapor). We obtained $D_m = 1.2 \times 10^{-12}$ m^2 s^{-1}, $dn_{PMMA}/dT = -1.1 \times 10^{-4}$ K^{-1}, $(\frac{dn}{dT})_m = -1.6\times10^{-4}\,\mathrm{K}^{-1}$ and $\alpha_{m,p}\frac{dC_{eq}}{dT} = -2.6\times10^{-5}\,\mathrm{K}^{-1}$ by fitting the FD-PBD data using the 20× objective lens.

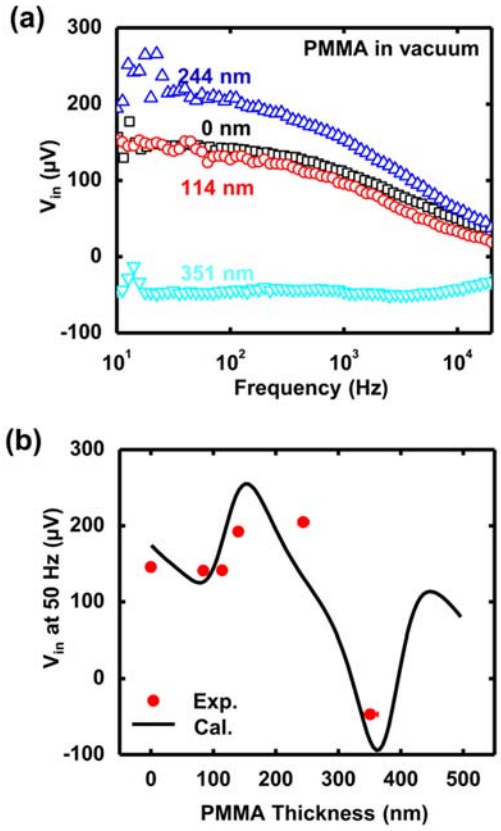

FIG. 5. (a) Representative in-phase signals measured on a series of PMMA/Al/a-SiO_2 samples placed in vacuum by FD-PBD with a 5× objective lens. The PMMA thickness of each sample is labeled. (b) The in-phase signals at 50 Hz for the PMMA/Al/a-SiO_2 samples as a function of the PMMA thicknesses. The red dots are measured data and the black curve is a calculation based on the multilayer optical model. Error bars for the measured PMMA thicknesses are included in the plot.

The magnitude of the FD-PBD signal strongly depends on the thickness of the polymer layer L_p. When L_p is much smaller than the laser wavelength, the magnitude of the signal correlates positively with L_p. The dependence of the signals on L_p becomes complicated because of optical interference effects as L_p becomes comparable to a fraction of the laser wavelength.[43] Figure 5(a) shows V_{in} of the FD-PBD signals measured on a series of PMMA/Al/a-SiO_2 samples with different PMMA thicknesses. The sample

was placed in vacuum, and the measurement used a 5× objective lens with a pump power of 3 mW and a probe power of 6 mW. To better compare with the calculation, we extracted the V_{in} at 50 Hz and plotted the data as a function of the PMMA thickness in Fig. 5(b). The beam deflection model (black curve) captures the optical interference effects and matches well with the measurements given all the complexity.

When the sample is placed in contact with water vapor at 0.38 psi, the relative magnitude of the FD-PBD signals also depend on the thickness of the polymer layer. Figure 6(a) and 6(b) shows the V_{out} components of the beam deflection signals measured on a series of PMMA/Al/a-SiO_2 and CA/Al/a-SiO_2 samples with different PMMA and CA thicknesses, respectively. The measurements used a 20× objective lens with a ratio of the pump power to the probe power of 1:2. The pump power varies from 1 mW to 2 mW depending on the thickness of the polymer to keep the steady-state heating roughly at 14 K. The positions of the frequency f_C that correspond to mass diffusion shift to higher frequency as the polymer thickness decreases. We further extracted f_C for each sample and plot f_C as a function of polymer thickness (L_p) in Fig. 6(c). We observe an inverse dependence of f_C on L_P^2, which is consistent with the expected behavior based on mass diffusion.

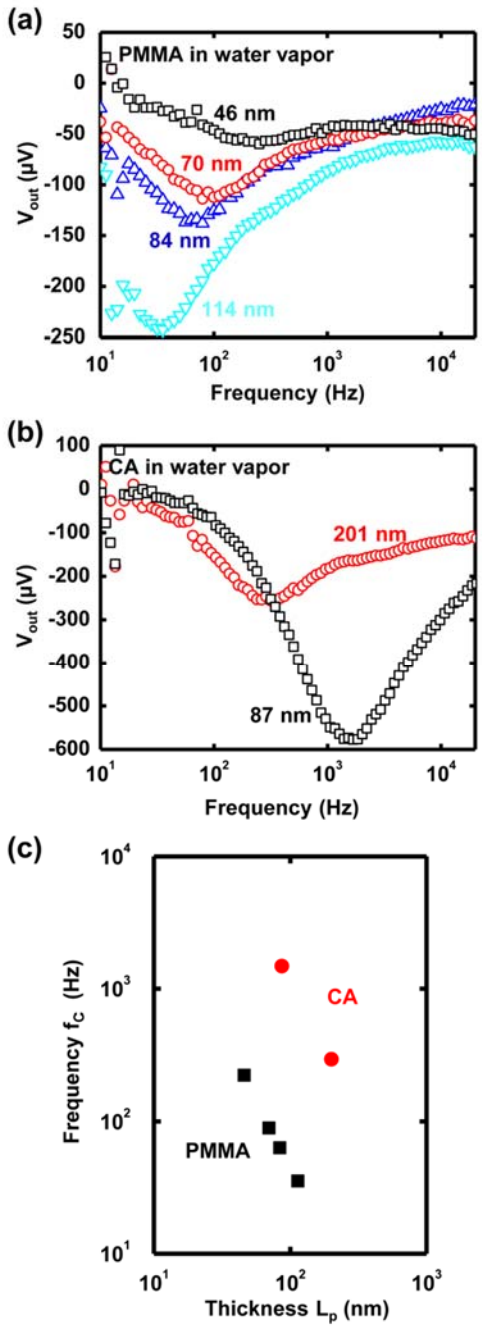

FIG. 6. (a) The out-of-phase component of the FD-PBD signals measured on a series of PMMA/Al/a-SiO_2 samples with various PMMA thicknesses. (b) The out-of-phase beam deflection signals obtained on two CA/Al/a-SiO2 samples with different CA thicknesses. (c) The

frequency f_C that corresponds to the minimum out-of-phase deflection signals as a function of the thickness of the polymer films L_p.

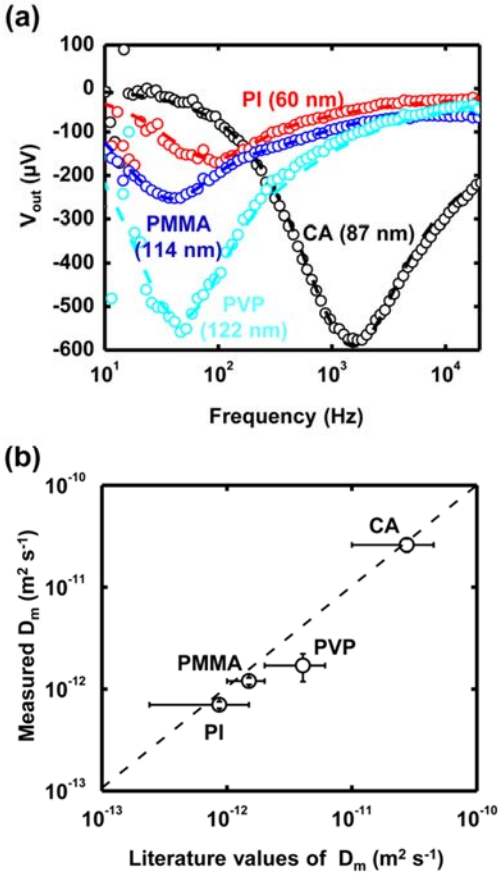

FIG. 7. (a) Out-of-phase signals of the deflection angles measured from PI/Al/a-SiO_2, PMMA/Al/a-SiO_2, PVP/Al/a-SiO_2 and CA/Al/a-SiO_2 by FD-PBD. Dashed lines correspond to the best fit based on the beam deflection model. (b) Comparison of the D_m measured by FD-PBD with literature values for the selected polymer films. The horizontal error bars represent the spread in literature values.

To further validate the effectiveness of FD-PBD for the measurement of water vapor diffusivity, we applied FD-PBD to several selected polymer thin films, and compared the measured D_m with literature values. The polymer films we studied include PI (60nm), PMMA (114nm), PVP (122nm) and CA (87nm). For this set of measurements,

we used a 20× objective lens, a pump power of 1 mW, a probe power of 2 mW and a water vapor pressure of 0.38 psi. The V_{out} component of the deflection signals (circles) as well as the fitting (dashed curves) based on the deflection model appear in Fig. 7(a). The fitted D_m is plotted in Fig. 7(b) against the corresponding literature values measured on micron-scale polymer films. Specifically, $D_m = 7.0\pm0.5 \times 10^{-13}$ m^2 s^{-1} for PI, $D_m = 1.2\pm0.1 \times 10^{-12}$ m^2 s^{-1} for PMMA, $D_m = 1.7\pm0.5 \times 10^{-12}$ m^2 s^{-1} for PVP and $D_m = 2.6\pm0.4 \times 10^{-11}$ m^2 s^{-1} for CA. We found that there are large discrepancies among the reported diffusivity from the literature for PI[8, 44, 45], PMMA[10, 41, 42], PVP[10, 46] and CA[47-49]. These discrepancies are plotted as the horizontal error bars for the literature values in Fig. 7(b).

V. WATER VAPOR DIFFUSIVITY IN NANOSCALE POLYMER FILMS AS A FUNCTION OF WATER VAPOR PRESSURE

Previous techniques for the measurement of mass diffusivity in polymer films require film thickness larger than tens of micrometers. Therefore, they are inapplicable to probe films with nanometer-scale thicknesses, such as the active layer of composite membranes typically used for separations. Moreover, most of the previous techniques operate under far-from-equilibrium conditions where the water concentration in the sample changes strongly with time and depth in the polymer film. A diffusivity averaged over a wide range of time and depth is often reported. However, the average diffusivity is not a good representation of the diffusion kinetics if the diffusivity changes significantly with water concentration.

As a further demonstration of the capability of FD-PBD, we measured the diffusivity of a PMMA film and the PIP/TMC film under various water vapor pressures. While PMMA is a dense hydrophobic polymer, PIP/TMC is a polyamide membrane

made by self-limiting interfacial polymerization. Because the chair structure of the PIP monomer does not allow the polymer chains to pack tightly, PIP/TMC membranes possess free-volume that potentially allow for fast transport of water.[50] Due to the nanoscale thickness of PIP/TMC and related membrane materials, the water vapor diffusivity has not been measured previously.

Figure 8(a)-(b) show the V_{out} component of the deflection signals measured from PMMA (114 nm)/Al/a-SiO_2 and (PIP/TMC) (90 nm)/Al/a-SiO_2 samples under various water vapor pressures. For both samples, the magnitudes of deflections decrease as the water vapor pressures are reduced. The frequency positions f_C of the negative-going peak in V_{out} for the PMMA sample stay invariant with the change of water pressure. In contrast, f_C of the PIP/TMC sample shifts to higher frequency as the water vapor pressure increases.

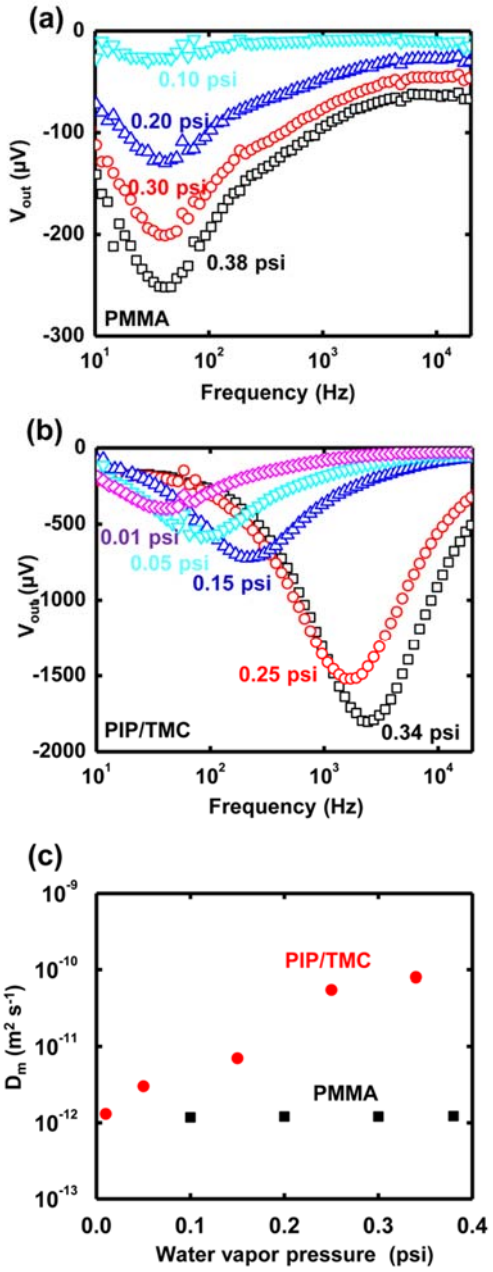

FIG. 8. (a)-(b) The out-of-phase component of the beam deflection signals measured on the PMMA/Al/a-SiO_2 and (PIP/TMC)/Al/a-SiO_2 samples, respectively. Different colors correspond to measurements under various water vapor pressures. (c) Measured D_m as a function of the water vapor pressure for the PMMA and PIP/TMC films.

We plot the extracted D_m for both samples as a function of the vapor pressure in Fig. 8(c). The extraction of D_m follows the deflection model and assumes that there is no resistance for water vapor diffusion in the water vapor layer under various pressures. As we expected, D_m of PMMA is nearly independent of hydration conditions. In contrast, D_m of PIP/TMC increases from $1x10^{-12}$ m^2 s^{-1} to $9x10^{-11}$ m^2 s^{-1} as the water vapor pressure increases from 0.02 psi to 0.38 psi. The nearly two-orders-of-magnitude increase in D_m is far beyond the uncertainty caused by the thickness change in the PIP/TMC membrane due to swelling (≈ 16% wt% at 100 RH).

The enhancement of water diffusion with the increased hydration level has been observed in glassy polymers (tens of microns thick) with relatively high water absorption. Such enhancement was attributed to either the increase in the free-volume in the water-polymer mixture, or to the plasticization of the polymer by the water content that favors the local chain dynamics.[10] This is also consistent with the much higher hydration level in the PIP/TMC film (≈ 16wt% under saturated water vapor at room temperature) than that in the PMMA film (≈ 2 wt% under saturated water vapor at room temperature[10]) that facilitates the creation of free-volume.

VI. DISCUSSION

We developed a laser-based technique to directly measure the water vapor diffusivity in polymer films of tens of nanometer thick. The measured diffusivity is categorized as the 'mutual-diffusion' coefficient which describes the diffusion under a concentration gradient (previously measured by FTIR-ATR and gravimetric methods) rather than the 'self-diffusion' coefficient which describes the random diffusion near

equilibrium (typically measured by nuclear magnetic resonance (NMR) and quasi-elastic neutron scattering (QENS)).[11] This is because a small perturbation of the water concentration is created by the small temperature excursion due to pump heating during the operation of FD-PBD.

Currently, the largest uncertainty for measured D_m comes from the uncertainty in determining the polymer thickness due to the swelling by water vapor. Spectroscopic ellipsometry measurements under controlled water vapor pressure and temperature could obtain accurate polymer thickness and reduce the uncertainty. Further reduction of the pointing instability of the laser beams by making the system more compact could effectively lower the overall noise floor of the measurement.

ACKNOWLEDGEMENTS

This work is supported by BP 75195/ICAM25. The sample preparation and measurement were carried out in part in the Frederick Seitz Materials Research Laboratory Central Research Facilities, University of Illinois.

*To whom correspondence should be addressed, (X.X.) E-mail: xiexuthu@gmail.com, (D.G.C.) E-mail: d-cahill@illinois.edu

APPENDIX A: Solution of the bi-directional heat diffusion in a layered structure

The temperature distribution in a layered structure in the spatial frequency domain (k) and temporal frequency domain (ω) is calculated by using the transfer matrix method.[28] Here both the top layer (i.e. layer 1) and the bottom layer (i.e., layer N) are

thermally thick and the heating source sits at the top surface of the layer h (i.e., metal transducer). Applying the Hankel transform and Fourier transform to the heat diffusion equation results in

$$\frac{\partial^2 T}{\partial z^2} - (4\pi^2 k^2 + \frac{i\omega}{D})T = 0 \quad . \qquad \text{(A.1)}$$

The solution can be expressed as a sum of thermal waves traveling forward and backward as in Eq. (2).

In the main text, we use the temperature of the top surface of the heating layer (i.e., $T_h(\mathrm{z}=0)$) to represent the temperature of the polymer film (i.e., T_p). This is valid since the temperature gradient in the vertical direction is negligible throughout the thin films within the range of heating frequency we used (i.e., 20 kHz to 10 Hz).

$$T_p \approx T_h(\mathrm{z}=0) = P\exp(-\pi^2 k^2 W_0^2 / 2) G_{tot} , \qquad \text{(A.2)}$$

where $P\exp(-\pi^2 k^2 W_0^2 / 2)$ is the heating power and $G_{\mathrm{tot}}(k,\omega)$ is the propagator for the layer h. To obtain G_{tot}, we first consider the heat propagating upward and downward separately.

$$\begin{pmatrix} A^+ \\ A^- \end{pmatrix}_{j+1} = \frac{1}{2\gamma_{j+1}} \begin{pmatrix} e^{u_{j+1}L_{j+1}} & 0 \\ 0 & e^{-u_{j+1}L_{j+1}} \end{pmatrix} \begin{pmatrix} \gamma_{j+1}+\gamma_j & \gamma_{j+1}-\gamma_j \\ \gamma_{j+1}-\gamma_j & \gamma_{j+1}+\gamma_j \end{pmatrix} \begin{pmatrix} A^+ \\ A^- \end{pmatrix}_j , \qquad \text{(A.3)}$$

$$\gamma_j = \Lambda_j u_j \qquad \text{(A.4)}$$

for the layer j iterating from 1 to h-2, where $A_1^- = 0$ and $A_1^+ = 1$ since heat cannot reach the other side of layer 1). The corresponding propagator is

$$G_{up} = \frac{1}{\gamma_{h-1}} \frac{A_{h-1}^{+} + A_{h-1}^{-}}{A_{h-1}^{+} - A_{h-1}^{-}}. \qquad \text{(A.5)}$$

For n that iterates from N to h+1,

$$\begin{pmatrix} B^{+} \\ B^{-} \end{pmatrix}_{j-1} = \frac{1}{2\gamma_{j-1}} \begin{pmatrix} e^{-u_{j-1}L_{j-1}} & 0 \\ 0 & e^{u_{j-1}L_{j-1}} \end{pmatrix} \begin{pmatrix} \gamma_{j-1} + \gamma_j & \gamma_{j-1} - \gamma_j \\ \gamma_{j-1} - \gamma_j & \gamma_{j-1} + \gamma_j \end{pmatrix} \begin{pmatrix} B^{+} \\ B^{-} \end{pmatrix}_{j}, \qquad \text{(A.6)}$$

where $B_N^{-} = 1$, $B_N^{+} = 0$ and the propagator is

$$G_{down} = \frac{1}{\gamma_h} \frac{B_h^{+} + B_h^{-}}{B_h^{+} - B_h^{-}}. \qquad \text{(A.7)}$$

G_{tot} is obtained by combining the heat flows downward and upward

$$G_{tot} = \frac{1}{1/G_{down} - 1/G_{up}}. \qquad \text{(A.8)}$$

The temperature vectors for the heat absorption layer and the layers below are (i.e. j from h to N)

$$\begin{pmatrix} \overline{T}^{+} \\ \overline{T}^{-} \end{pmatrix}_{j} = \frac{P \exp(-\pi^2 k^2 W_0^2 / 2) G_{tot}}{B_h^{+} + B_h^{-}} \begin{pmatrix} B_j^{+} \\ B_j^{-} \end{pmatrix}. \qquad \text{(A.9)}$$

The temperature vectors for layers above the heat absorption layer are

$$\begin{pmatrix} \overline{T}^{+} \\ \overline{T}^{-} \end{pmatrix}_{1} = \frac{P \exp(-\pi^2 k^2 W_0^2 / 2) G_{tot}}{A_{h-1}^{+} + A_{h-1}^{-}} \begin{pmatrix} A_1^{+} \\ A_1^{-} \end{pmatrix} \qquad \text{(A.10)}$$

for j=1, and

$$\begin{pmatrix} \overline{T}^{+} \\ \overline{T}^{-} \end{pmatrix}_{j} = \frac{P \exp(-\pi^2 k^2 W_0^2 / 2) G_{tot}}{A_{h-1}^{+} + A_{h-1}^{-}} \begin{pmatrix} e^{-u_n L_j} & 0 \\ 0 & e^{u_n L_j} \end{pmatrix} \begin{pmatrix} A_j^{+} \\ A_j^{-} \end{pmatrix} \qquad \text{(A.11)}$$

for the rest of layers (i.e. j from 2 to h-1).

APPENDIX B: Determining material properties used in the FD-PBD model

Table I lists the values of the material properties used in the FD-PBD model. These properties include the thermal conductivity (Λ), volumetric heat capacity (C_V), refractive index (n), temperature coefficient of the refractive index (or thermos-optic coefficient dn/dT), coefficient of thermal expansion (α_T) , Poisson's ratio (υ) and Young's modulus (Y).

TABLE I. Values of parameters used in the FD-PBD model

	Λ (W $m^{-1}K^{-1}$)	C_V (J $cm^{-3}K^{-1}$)	n	dn/dT (K^{-1})	α_T ($1x10^{-6}$ K^{-1})	υ	Y (GPa)
Water Vapor (21 Torr, 23°C)	0.019 (ref. [51])	$3.0x10^{-5}$	1.00	$-2.1x10^{-8}$ (ref. [52])	---	---	---
PMMA	0.19 ± 0.02 (ref. [53])	1.60± 0.15 (ref. [53])	1.49	$-0.78x10^{-4}$	33	0.37 (ref. [53])	3.2 (ref. [54])
Al	160	2.42	1.96 + 7.10i	$-1.6x10^{-3}$ + $3.1x10^{-4}$i	23 (ref. [26])	0.33 (ref. [55])	69 (ref. [56])
Fused Silica	1.32	1.63	---	---	0.54 (ref. [26])	0.17 (ref. [55])	73 (ref. [56])

The thermal conductivity and heat capacity of the water vapor are insignificant compared with those of the sample. Thereby, the water vapor only has negligible effects on the temperature distribution in the sample. We adopt the thermal conductivity (0.019 W m^{-1} K^{-1}) of the saturated water vapor at room temperature (RT) to solve the heat diffusion equation.[51] This value is consistent with the calculation based on the kinetic

theory and is nearly independent of the pressure within the pressure range used in our experiments. The heat capacity of the water vapor is proportional to the pressure. We estimated the heat capacity as 3×10^{-5} J K^{-1} cm^{-3} for the typical experimental condition (2.6×10^{3} Pa at RT). The thermo-optic coefficient of the water vapor (dn_{vap}/dT) is determined as -2.1×10^{-8} K^{-1} for our typical experimental conditions based on the measurements by Edlén. [52]

The thermal conductivity, the heat capacity, the Poisson's ratio and the Young's modulus of PMMA all come from literature values.[53, 54] The refractive index of PMMA was measured by applying spectroscopic ellipsometry on a PMMA thin film spin-coated on a Si substrate. We determined the expansion coefficient of PMMA α_T by measuring the beam deflection on a sample Al/PMMA (97 nm)/a-SiO_2, and used the FD-PBD model to fit the data with α_T as the only fitting parameter. The fitting from 10^2 Hz to 10^5 Hz yields $\alpha_T = 33 \times 10^{-6}$ K^{-1} for the PMMA. At low frequency (< 100Hz), the fitting is poor, presumably due to the relaxation of polymer chains at low frequency. Similarly, we obtained the thermo-optic coefficient of PMMA (dn_{PMMA}/dT) by fitting the beam deflection from a sample of PMMA (114 nm)/Al/a-SiO_2 with dn_{PMMA}/dT as the only parameter.

The refractive index of Al at λ = 783 nm was measured by spectroscopic ellipsometry as $n_{Al} = 1.96 + 7.10i$. This value is smaller than the literature value of 2.63 + 8.58i because we ignored the native oxide above the Al in fitting the ellipsometry data. $n_{Al} = 1.96 + 7.10i$ is used throughout the modeling for simplicity (we assumed zero thickness of Al_2O_3). The complex temperature dependence of n_{Al} (i.e. dn_{Al}/dT) is determined together by the temperature derivative of the reflectivity (dR/dT) and the

temperature derivative of the Fresnel coefficient (dϕ/dT) of a Al (80 nm)/a-SiO_2 sample measured in vacuum

$$\frac{dR}{2RdT} = \mathrm{Re}(2\frac{dn_{Al}/dT}{n_{Al}^2 - 1}), \qquad (A.12)$$

$$\frac{d\phi}{dT} = \mathrm{Im}(2\frac{dn_{Al}/dT}{n_{Al}^2 - 1}), \qquad (A.13)$$

Where 'Re' and 'Im' are the functions that take the real part and imaginary part of a complex number, respectively, R=0.87 and dR/dT $\approx$ 1×10^{-4} K^{-1} come from TDTR measurements, and dϕ/dT=2×10^{-5} K^{-1} is obtained by fitting the FD-PBD data using the model with dϕ/dT as the only fitting parameter. We found that $dn_{Al}/dT = -1.6\times10^{-3} + 3.1\times10^{-4}i$.

The thermal conductivity of the Al transducer was determined by the Wiedemann-Franz law based on the electrical conductivity measured by a four-point probe system. The thermal conductivity of the a-SiO_2 was measured by TDTR. We used the literature values for the heat capacity, the Possion's ratio and the Young's modulus of Al and a-SiO_2.[26, 55, 56]

APPENDIX C: Modeling contributions to the beam deflection from each mechanism

The sample geometry used for the simulation of beam deflections in Fig. 2 is PMMA (100 nm)/ Al (80nm)/ a-SiO_2 (infinite thickness). A pump power of 3mW, a spot size of 11μm and a pump-probe separation of 12 μm correspond to the case of using a 5× objective lens.

When calculating θ_{nC}, we only considered the changes in the refractive index of the polymer due to the water concentration field, while excluding all other contributions

(i.e. only calculate Z_0 with $\frac{dn_p}{dC_{\mathrm{eq}}}\frac{dC_{\mathrm{eq}}}{dT} = -1\times10^{-4}\,\mathrm{K}^{-1}$, while $\alpha_{\mathrm{m},p}\frac{dC_{\mathrm{eq}}}{dT}$ for the polymer layer, α_{T} and $\frac{dn}{dT}$ for all the layers are set to zero). Likewise, we only use the expansion of the polymer due to the water concentration field when calculating θ_{LC} (i.e. set $\alpha_{\mathrm{m},p}\frac{dC_{\mathrm{eq}}}{dT} = -2\times10^{-5}\,\mathrm{K}^{-1}$ while $\frac{dn_p}{dC_{\mathrm{eq}}}\frac{dC_{\mathrm{eq}}}{dT} = 0$ for the polymer layer and $\alpha_{\mathrm{T}} = \frac{dn}{dT} = 0$ for all the layers in computing Z_0).

θ_{LT} was obtained by computing Z_0 in the model with parameters $\alpha_{\mathrm{T},p} = 33\times10^{-6}\,\mathrm{K}^{-1}$, $\frac{dn_p}{dC_{\mathrm{eq}}}\frac{dC_{\mathrm{eq}}}{dT} = \alpha_{\mathrm{m},p}\frac{dC_{\mathrm{eq}}}{dT} = \frac{dn}{dT} = 0$. To determine θ_{nT}, we only considered $\frac{dn}{dT}$ of the sample in the optical transfer matrix and ignored all other mechanisms that cause the beam deflection.

APPENDIX D: Calibration of the frequency-dependent amplitude variation and phase shifts of the system

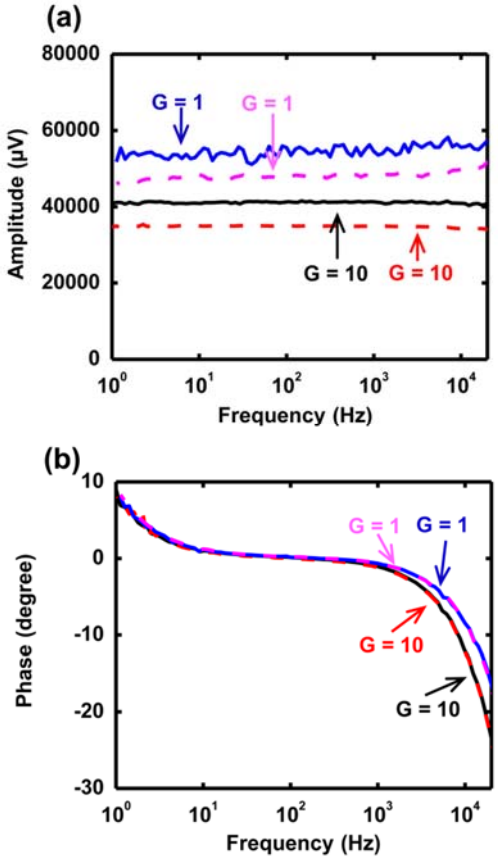

FIG. A1. (a)-(b) Calibration curves of the frequency-dependence of the amplitude (a) and phase (b) response of the measurement system. Black lines and red dashed lines are two measurements corresponding to the second stage gain of the quadrature detector $G = 10$. Blue lines and magenta dashed lines are two measurements corresponding to the second stage gain $G = 1$.

APPENDIX E: Sensitivity analysis

The sensitivity parameter S_γ for the measured signal (f_C) is defined as

$$S\_\gamma = \frac{\partial \ln(f_C)}{\partial \ln(\alpha)}, \qquad \text{(A. 14)}$$

where γ is one of the key parameters in the model, such as W_0 (in our experiments $W_0 = W_1$), r_0, D_m and L_p. The sensitivity as a function of corresponding parameters appears in

Fig. A2. Basic parameters used in the calculation are: $W_1 = W_0 = 2.7$ μm, $r_0 = 4$ μm, $D_m = 1.1\times10^{-12}$ m^2 s^{-1}, $\frac{dn_p}{dC_{eq}}\frac{dC_{eq}}{dT} = -1.6\times10^{-4}\,K^{-1}$, $\alpha_{m,p}\frac{dC_{eq}}{dT} = -2.6\times10^{-5}\,K^{-1}$, $\alpha_{T,p} = 33\times10^{-6}\,K^{-1}$ and $\frac{dn_p}{dT} = -1.1\times10^{-4}\,K^{-1}$. To calculate S_γ, we vary the value of γ and keep all other parameters the same.

While f_C is most sensitive to L_p ($S\_L_p \sim -2$) and D_m ($S\_D_m \sim 1$), the sensitivity of f_C to W_0, W_1 and r_0 is close to zero.

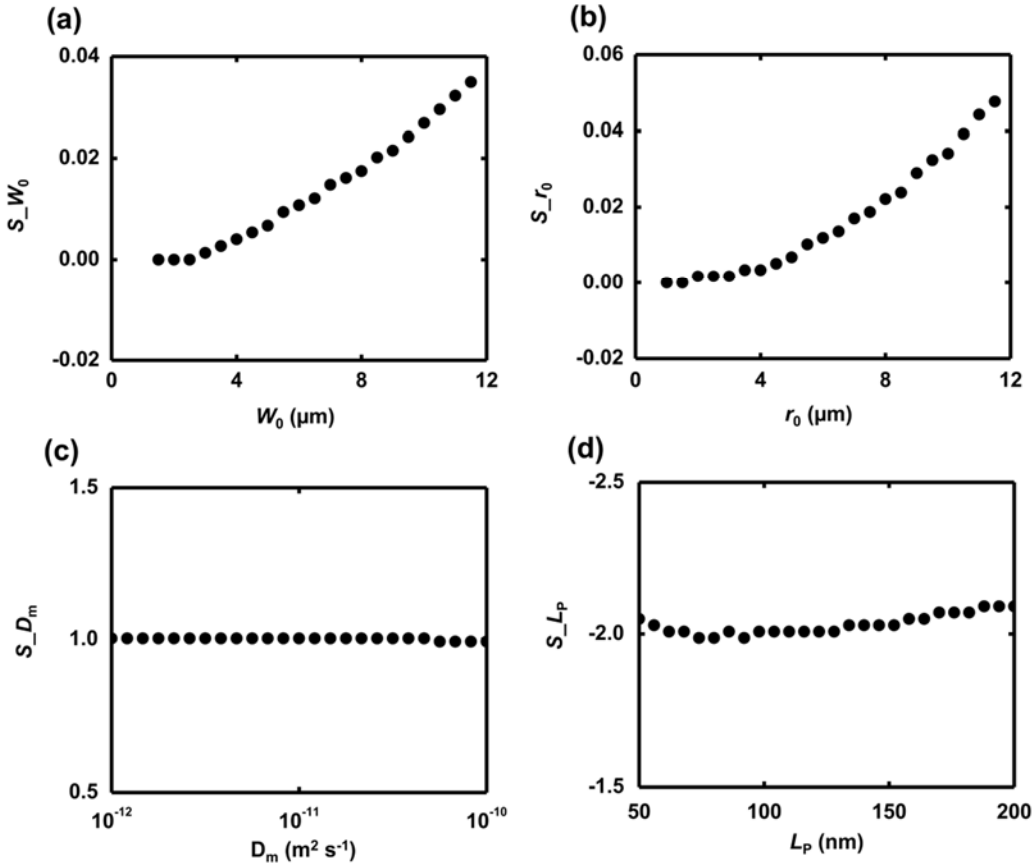

FIG. A2. (a)-(d) Sensitivity of f_C with respect to the laser spot size W_0 (a), pump-probe separation r_0 (b), mass diffusivity D_m (c) and the polymer thickness L_p (d).

References

[1] R. Auras, B. Harte, and S. Selke, Macromol. Biosci. **4**, 835 (2004).
[2] C. P. Wong, Adv. Polym. Sci. **84**, 63 (1988).
[3] S. Kirsten, J. Wetterling, J. Uhlemann, K. J. Wolter, and S. Zigler, 2013 IEEE XXIII International Scientific Conference Electronics and Nanotechnology (Elnano), 269 (2013).
[4] K. A. Mauritz and R. B. Moore, Chem. Rev. **104**, 4535 (2004).
[5] Y. Yampolskii, Macromolecules **45**, 3298 (2012).
[6] R. W. Baker and B. T. Low, Macromolecules **47**, 6999 (2014).
[7] C. M. Balik, Macromolecules **29**, 3025 (1996).
[8] K. I. Okamoto, N. Tanihara, H. Watanabe, K. Tanaka, H. Kita, A. Nakamura, Y. Kusuki, and K. Nakagawa, J. Polym. Sci. B Polym. Phys. **30**, 1223 (1992).
[9] M. G. De Angelis, S. Lodge, M. G. Baschetti, G. C. Sarti, F. Doghieri, A. Sanguineti, and P. Fossati, Desalination **193**, 398 (2006).
[10] E. M. Davis and Y. A. Elabd, J. Phys. Chem. B **117**, 10629 (2013).
[11] D. T. Hallinan and Y. A. Elabd, J. Phys. Chem. B **113**, 4257 (2009).
[12] K. C. Farinas, L. Doh, S. Venkatraman, and R. O. Potts, Macromolecules **27**, 5220 (1994).
[13] J. Harmon, C. Coffman, S. Villarrial, S. Chabolla, K. A. Heisel, and V. V. Krishnan, J. Chem. Educ. **89**, 780 (2012).
[14] J. H. Zhang, M. V. Giotto, W. Y. Wen, and A. A. Jones, J. Membr. Sci. **269**, 118 (2006).
[15] A. A. Pivovar and B. S. Pivovar, J. Phys. Chem. B **109**, 785 (2005).
[16] V. Pilla, E. Munin, and M. R. R. Gesualdi, J. Opt. A: Pure Appl. Opt. **11**, 105201 (2009).
[17] P. R. B. Pedreira, L. Hirsch, J. R. D. Pereira, A. N. Medina, A. C. Bento, and M. L. Baesso, Rev. Sci. Instrum. **74**, 808 (2003).
[18] A. R. Sadrolhosseini, A. S. M. Noor, L. A. Mehdipour, A. Noura, and M. A. Mahdi, Opt Rev **22**, 289 (2015).
[19] E. T. Ogawa, C. A. Hu, and P. S. Ho, J. Appl. Phys. **86**, 6018 (1999).
[20] A. Koniger, H. Wunderlich, and W. Kohler, J. Chem. Phys. **132**, 174506 (2010).
[21] A. Koniger, B. Meier, and W. Kohler, Philos. Mag. **89**, 907 (2009).
[22] M. N. S. Swapna, M. J. Anitha, and S. I. Sankararaman, J. Biomed. Opt. **22**, 068001 (2017).
[23] C. Barbero, M. C. Miras, R. Kotz, and O. Haas, Solid State Ion. **60**, 167 (1993).
[24] A. G. Brolo and S. D. Sharma, Electrochim. Acta **48**, 1375 (2003).
[25] S. A. Putnam and D. G. Cahill, Rev. Sci. Instrum. **75**, 2368 (2004).
[26] X. Zheng, D. G. Cahill, R. Weaver, and J. C. Zhao, J. Appl. Phys. **104**, 073509 (2008).
[27] X. Xie, X. Zheng, R. Weaver, J. C. Zhao, and D. G. Cahill, J. Appl. Phys. **122**, 219901 (2017).
[28] D. G. Cahill, Rev. Sci. Instrum. **75**, 5119 (2004).
[29] J. G. Wijmans and R. W. Baker, J. Membr. Sci. **107**, 1 (1995).
[30] G. Chen, *Nanoscale energy transport and conversion : a parallel treatment of electrons, molecules, phonons, and photons* (Oxford University Press, Oxford ; New York, 2005).
[31] G. R. Fowles, *Introduction to modern optics* (Dover Publications, New York, 1989).
[32] J. Oishi and T. Kimura, Metrologia **5**, 50 (1969).
[33] S. J. Park, W. Choi, S. E. Nam, S. Hong, J. S. Lee, and J. H. Lee, J. Membr. Sci. **526**, 52 (2017).
[34] X. Xie, D. Y. Li, T. H. Tsai, J. Liu, P. V. Braun, and D. G. Cahill, Macromolecules **49**, 972 (2016).

[35] K. Kang, Y. K. Koh, C. Chiritescu, X. Zheng, and D. G. Cahill, Rev. Sci. Instrum. **79**, 114901 (2008).
[36] A. J. Schmidt, R. Cheaito, and M. Chiesa, Rev. Sci. Instrum. **80**, 094901 (2009).
[37] J. P. Feser, J. Liu, and D. G. Cahill, Rev. Sci. Instrum. **85**, 104903 (2014).
[38] H. K. Lonsdale, U. Merten, and R. L. Riley, J. Appl. Polym. Sci. **9**, 1341 (1965).
[39] R. S. Moshrefzadeh, M. D. Radcliffe, T. C. Lee, and S. K. Mohapatra, J. Light. Technol. **10**, 420 (1992).
[40] G. Beadie, M. Brindza, R. A. Flynn, A. Rosenberg, and J. S. Shirk, Appl. Opt. **54**, F139 (2015).
[41] D. T. Turner, Polymer **23**, 197 (1982).
[42] I. Linossier, F. Gaillard, M. Romand, and J. F. Feller, J. Appl. Polym. Sci. **66**, 2465 (1997).
[43] J. Opsal, A. Rosencwaig, and D. L. Willenborg, Appl. Opt. **22**, 3169 (1983).
[44] J. Seo and H. Han, J. Appl. Polym. Sci. **82**, 731 (2001).
[45] M. Metayer, M. Labbe, S. Marais, D. Langevin, C. Chappey, F. Dreux, M. Brainville, and P. Belliard, Polym. Test **18**, 533 (1999).
[46] O. Rodriguez, F. Fornasiero, A. Arce, C. J. Radke, and J. M. Prausnitz, Polymer **44**, 6323 (2003).
[47] P. P. Roussis, Polymer **22**, 1058 (1981).
[48] M. J. Palin, G. J. Gittens, and G. B. Porter, J. Appl. Polym. Sci. **19**, 1135 (1975).
[49] F. A. Long and L. J. Thompson, J Polym Sci **15**, 413 (1955).
[50] J. Jegal, S. G. Min, and K. H. Lee, J. Appl. Polym. Sci. **86**, 2781 (2002).
[51] K. I. Amirkhanov, A. P. Adamov, and U. B. Magomedov, J. Eng. Phy. **34**, 141 (1978).
[52] B. Edlén, Metrologia **2**, 71 (1965).
[53] X. Xie, K. X. Yang, D. Y. Li, T. H. Tsai, J. Shin, P. V. Braun, and D. G. Cahill, Phys. Rev. B **95**, 035406 (2017).
[54] J. M. Torres, C. M. Stafford, and B. D. Vogt, ACS Nano **3**, 2677 (2009).
[55] G. N. Greaves, A. L. Greer, R. S. Lakes, and T. Rouxel, Nat. Mater. **10**, 823 (2011).
[56] M. de Jong, et al., Sci. Data **2**, 150009 (2015).

Figure 1

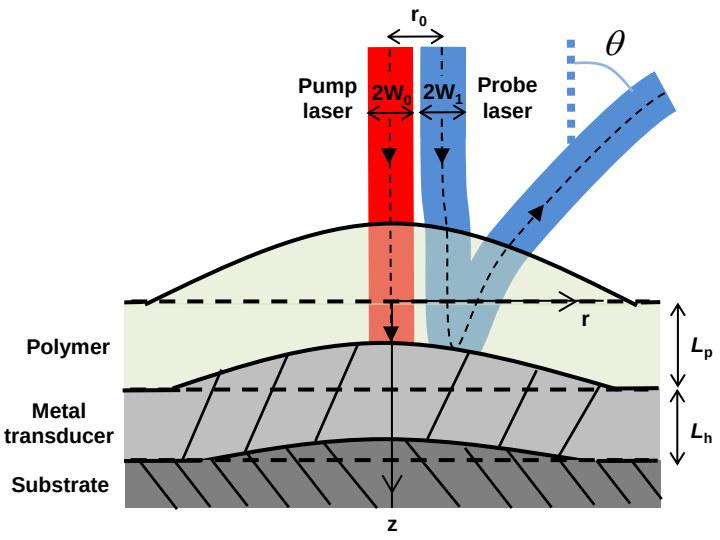
r0
θ
Pump laser
2W0
2W1
Probe laser
r
Polymer
Metal transducer
Substrate
Lp
Lh
z

Figure 2

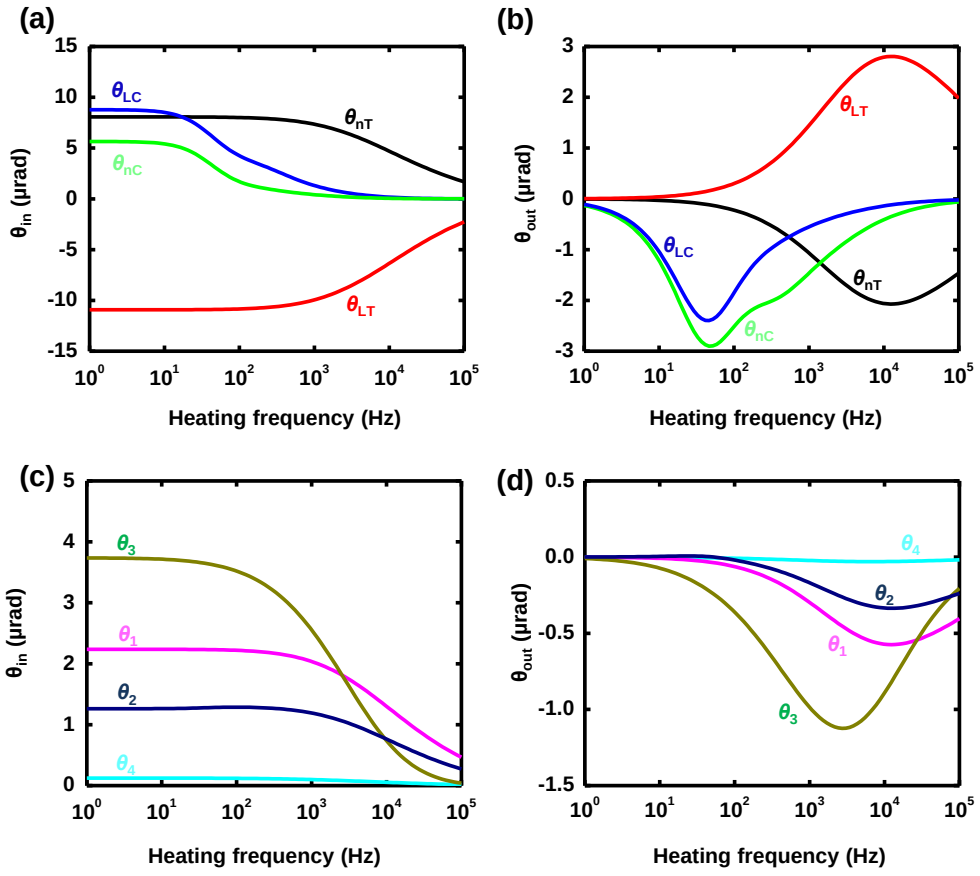
(a)
θin (μrad)
θLC
θnT
θnC
θLT
Heating frequency (Hz)
(b)
θout (μrad)
θLT
θLC
θnT
θnC
Heating frequency (Hz)
(c)
θin (μrad)
θ3
θ1
θ2
θ4
Heating frequency (Hz)
(d)
θout (μrad)
θ4
θ2
θ1
θ3
Heating frequency (Hz)

Figure 3

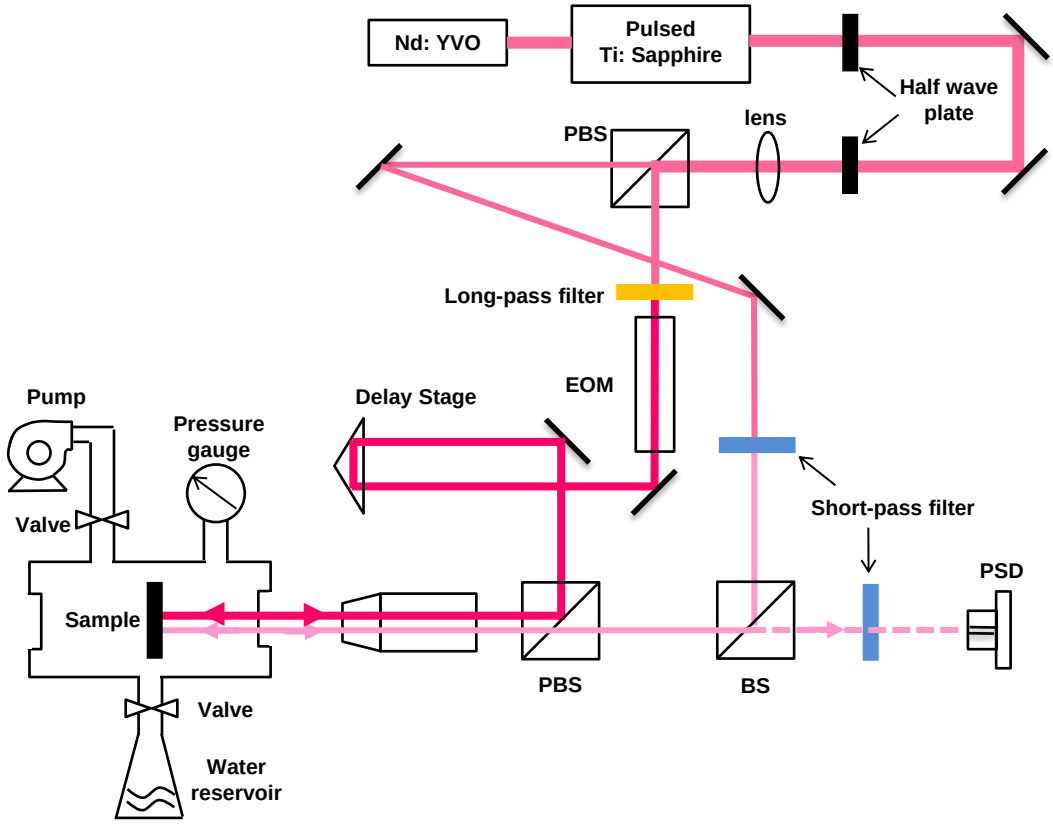
Nd: YVO
Pulsed
Ti: Sapphire
Half wave
plate
lens
PBS
Long-pass filter
EOM
Delay Stage
Pump
Pressure
gauge
Valve
Short-pass filter
PSD
Sample
PBS
BS
Valve
Water
reservoir

Figure 4

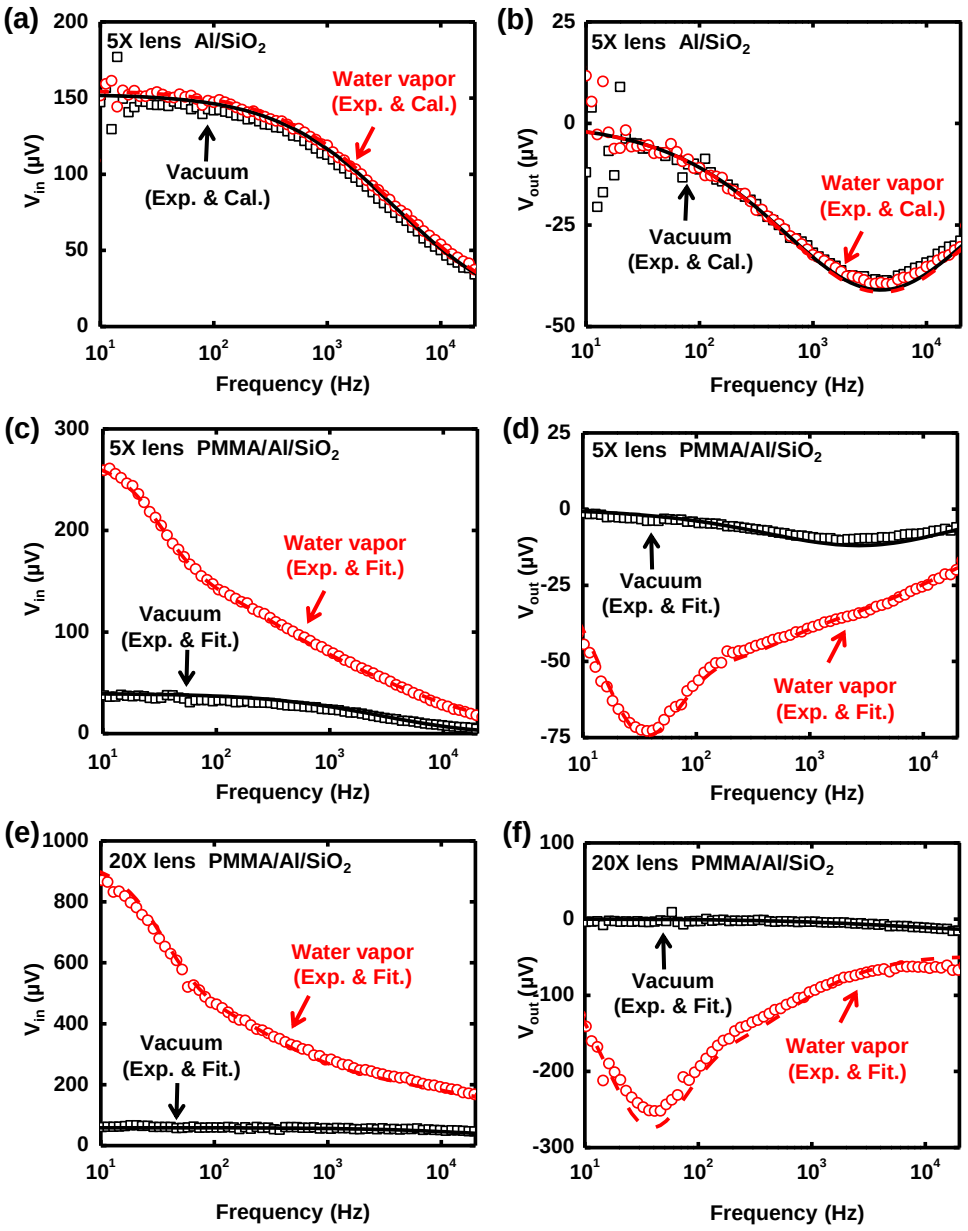
(a)
5X lens Al/SiO2
Water vapor
(Exp. & Cal.)
Vacuum
(Exp. & Cal.)
Vin (μV)
Frequency (Hz)
(b)
5X lens Al/SiO2
Water vapor
(Exp. & Cal.)
Vacuum
(Exp. & Cal.)
Vout (μV)
Frequency (Hz)
(c)
5X lens PMMA/Al/SiO2
Water vapor
(Exp. & Fit.)
Vacuum
(Exp. & Fit.)
Vin (μV)
Frequency (Hz)
(d)
5X lens PMMA/Al/SiO2
Vacuum
(Exp. & Fit.)
Water vapor
(Exp. & Fit.)
Vout (μV)
Frequency (Hz)
(e)
20X lens PMMA/Al/SiO2
Water vapor
(Exp. & Fit.)
Vacuum
(Exp. & Fit.)
Vin (μV)
Frequency (Hz)
(f)
20X lens PMMA/Al/SiO2
Vacuum
(Exp. & Fit.)
Water vapor
(Exp. & Fit.)
Vout (μV)
Frequency (Hz)

Figure 5

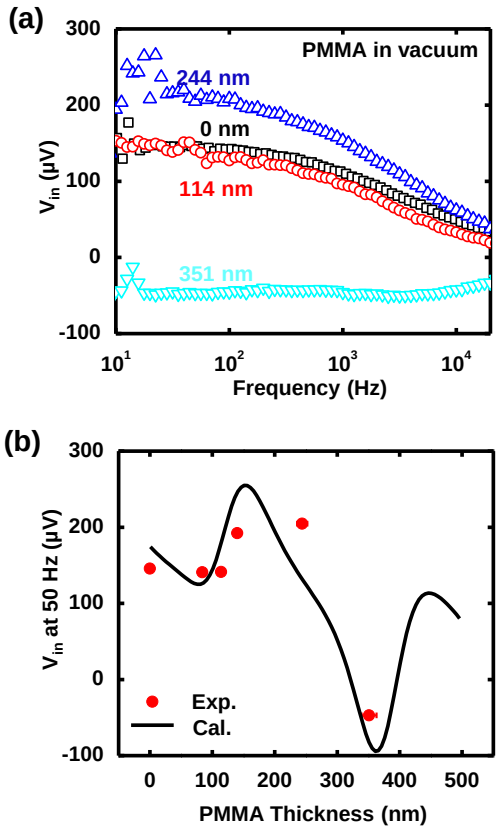
(a)
PMMA in vacuum
244 nm
0 nm
114 nm
351 nm
V_{in} (μV)
Frequency (Hz)
(b)
V_{in} at 50 Hz (μV)
Exp.
Cal.
PMMA Thickness (nm)

Figure 6

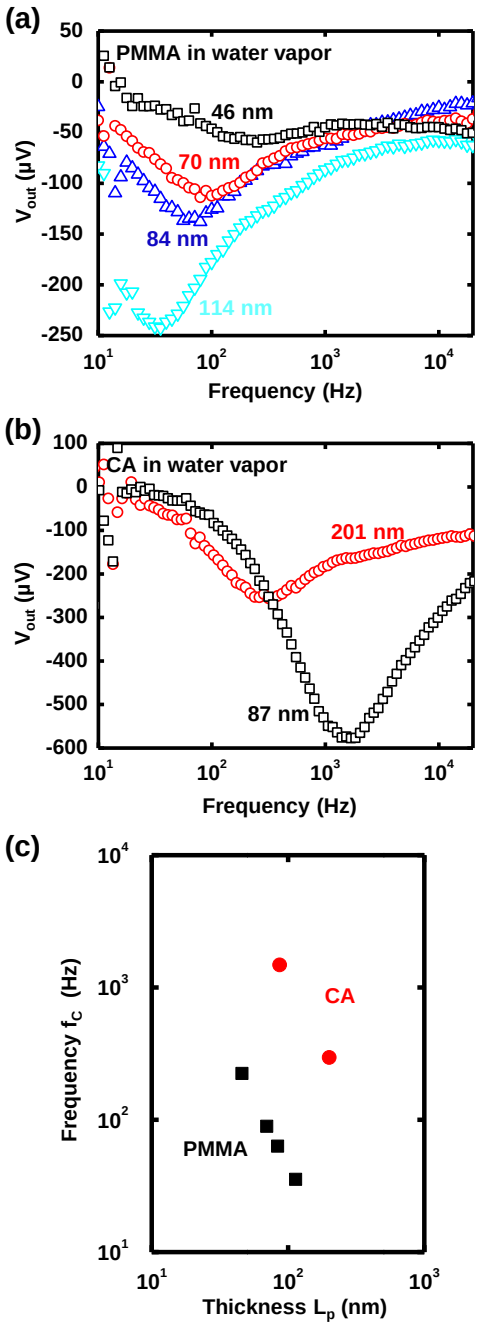
(a)
PMMA in water vapor
46 nm
70 nm
84 nm
114 nm
V_{out} (μV)
Frequency (Hz)
(b)
CA in water vapor
201 nm
87 nm
V_{out} (μV)
Frequency (Hz)
(c)
CA
PMMA
Frequency f_C (Hz)
Thickness L_p (nm)

Figure 7

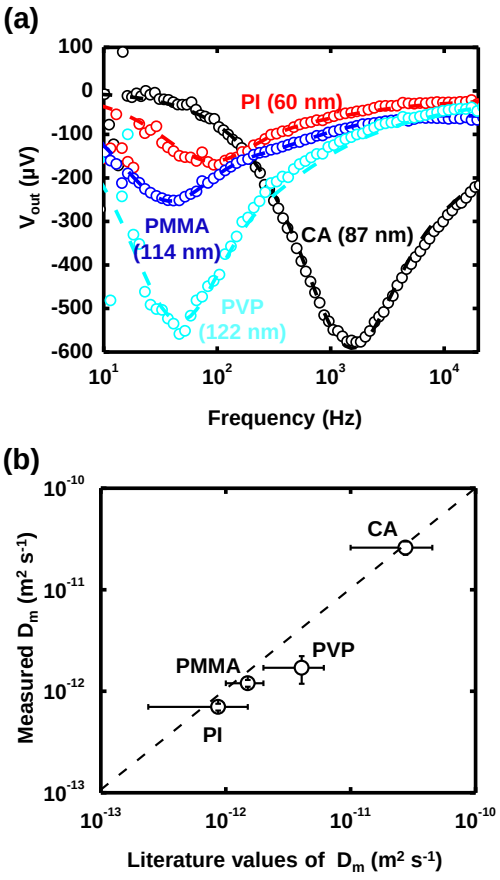
(a)
100
0
-100
-200
-300
-400
-500
-600
V_{out} (μV)
PI (60 nm)
PMMA
(114 nm)
CA (87 nm)
PVP
(122 nm)
10^1
10^2
10^3
10^4
Frequency (Hz)
(b)
10^{-10}
10^{-11}
10^{-12}
10^{-13}
Measured D_m (m^2 s^{-1})
CA
PMMA
PVP
PI
10^{-13}
10^{-12}
10^{-11}
10^{-10}
Literature values of D_m (m^2 s^{-1})

Figure 8

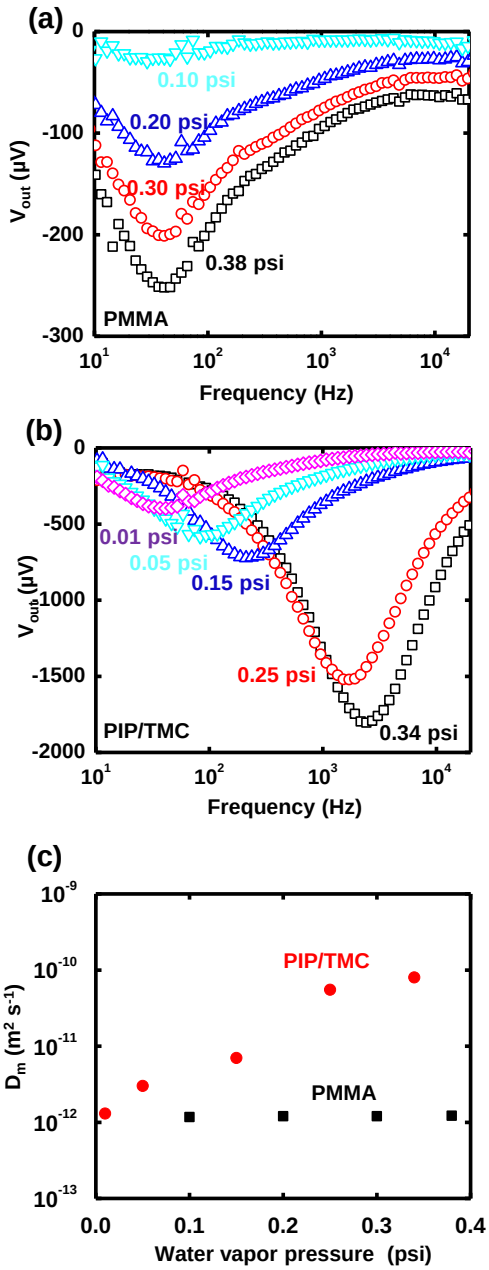
(a)
0.10 psi
0.20 psi
0.30 psi
0.38 psi
PMMA
V_{out} (μV)
Frequency (Hz)
(b)
0.01 psi
0.05 psi
0.15 psi
0.25 psi
0.34 psi
PIP/TMC
V_{out} (μV)
Frequency (Hz)
(c)
PIP/TMC
PMMA
D_m (m^2 s^{-1})
Water vapor pressure (psi)

Figure A1

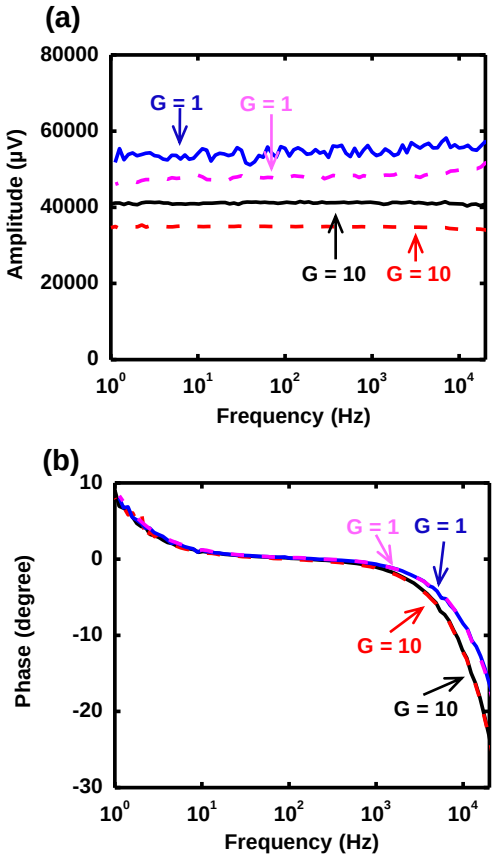
(a)
80000
60000
40000
20000
0
Amplitude (μV)
G = 1
G = 1
G = 10
G = 10
10^0
10^1
10^2
10^3
10^4
Frequency (Hz)
(b)
10
0
-10
-20
-30
Phase (degree)
G = 1
G = 1
G = 10
G = 10
10^0
10^1
10^2
10^3
10^4
Frequency (Hz)

Figure A2

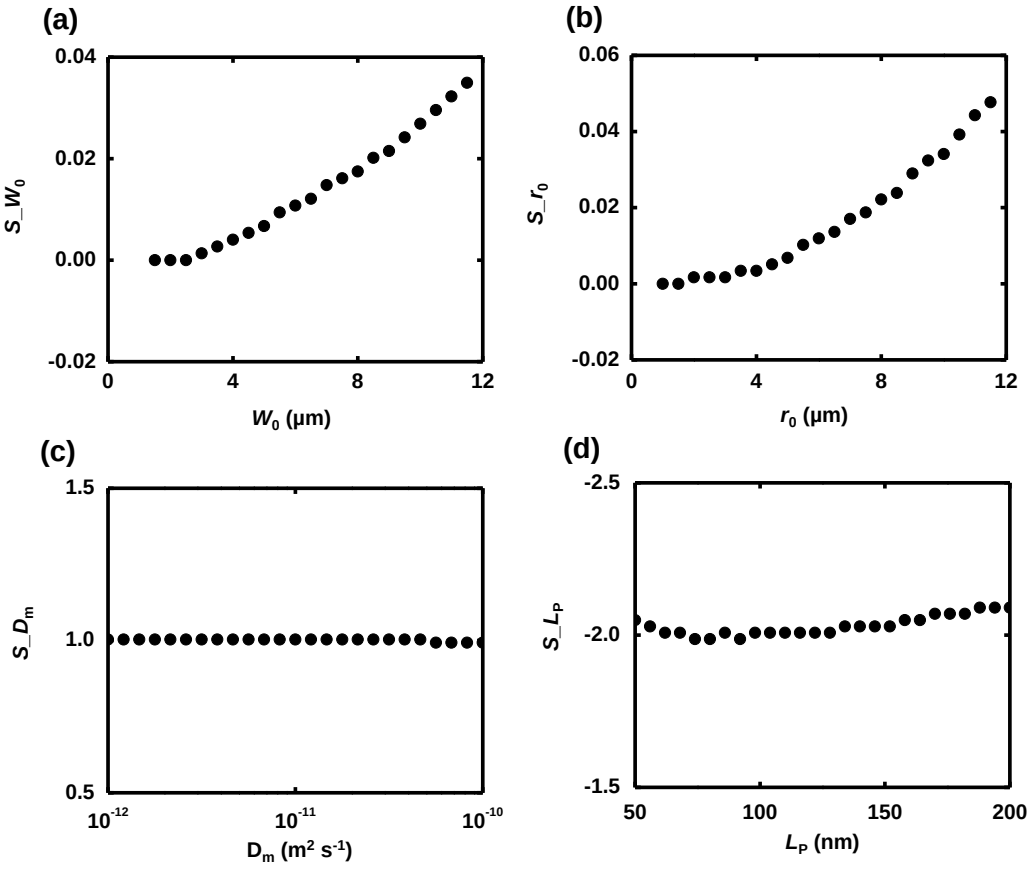
(a)
0.04
0.02
0.00
-0.02
S_W0
0
4
8
12
W0 (μm)
(b)
0.06
0.04
0.02
0.00
-0.02
S_r0
0
4
8
12
r0 (μm)
(c)
1.5
1.0
0.5
S_Dm
10-12
10-11
10-10
Dm (m2 s-1)
(d)
-2.5
-2.0
-1.5
S_LP
50
100
150
200
LP (nm)